THESIS FOR THE DEGREE OF LICENTIATE OF ENGINEERING

Ionic Liquid-Based Electrolytes for High-Temperature Lithium-Metal Batteries

QUAN WU

Department of Physics

CHALMERS UNIVERSITY OF TECHNOLOGY

Gothenburg, Sweden 2025

Ionic Liquid-Based Electrolytes for High-Temperature Lithium-Metal Batteries

QUAN WU

Department of Physics
Chalmers University of Technology
SE-412 96 Gothenburg
Sweden
Telephone + 46 (0)31-772 1000

Cover:
[Electrolyte Design for Ionic Liquid-Based Electrolytes for High-Temperature Lithium-Metal Batteries]

Chalmers Digitaltryck
Gothenburg, Sweden 2025

Ionic Liquid-Based Electrolytes for High-Temperature Lithium-Metal Batteries

QUAN WU

Department of Physics

Chalmers University of Technology

Abstract

Lithium metal batteries are promising candidates for high-energy-density electrochemical energy storage systems due to the low redox potential and high theoretical capacity of Li metal anodes. However, their practical application, especially at high temperatures, is hindered by unstable Li deposition, dendrite growth, side reactions, and rapid interfacial degradation, which compromise Coulombic efficiency, cycle life, and safety. These challenges are closely linked to the interfacial processes governing Li^+ transport, desolvation, structure of the electric double layer, solid electrolyte interphase (SEI), and nucleation/growth of Li-metal at the surface. In this thesis, two electrolyte engineering strategies were used to address these issues by tuning the Li^+ solvation structure, ionic transport, and interfacial processes. First, a novel ionic liquid electrolyte (NS-DAIL) was designed by incorporating $LiNO_3$ and sulfolane into a dual-anion ionic liquid electrolyte, which weakens the Li^+-anion coordination, reduces the desolvation barrier, and enhances Li^+ transfer kinetics, enabling uniform Li plating and improved rate performance at high temperature. Second, by introducing an ionic liquid ($Pyr_{14}FSI$) as an additive into a conventional carbonate electrolyte, the electrode-electrolyte interface is modified, delaying Li^+ depletion at the interface during plating, which mitigates dendrite growth. These two studies elucidate the interplay between solvation structure, ionic transfer kinetics, SEI properties, and suppression of dendrite growth, providing mechanistic insights and practical strategies for achieving safe, high-performance, high-temperature lithium metal batteries.

Keywords: High-temperature lithium metal batteries, ionic liquid electrolyte, solvation structure, solid electrolyte interphase (SEI)

List of Papers

1. **Q. Wu**, C. Cardona, A. Persdotter, N. Abdou, S. Xiong, P. Johansson, F. Liu, A. Martinelli, L. Evenäs, A. Matic, "A Weak Anion-Coordination Ionic Liquid Electrolyte for High-Temperature Li-Metal Batteries" (In manuscript)

2. **Q. Wu**, A. Persdotter, J. Jamroz, A. Matic, "Interfacial Reconstruction via Ionic Liquid Additives Enables Dendrite-Free High-Temperature Lithium-Metal Batteries" (In manuscript)

3. **Q. Wu**, E. D. Esping, M. Afiandika, S. Xiong, A. Matic, "Understanding the electro-chemo-mechanics of lithium metal anodes" *eScience* 2025, 100429.

Contribution Report

Paper I:
Q. Wu: conceptualization, investigation, methodology, data curation, visualization, writing - original draft, writing - review& editing.
C. Cardona: MD simulation, writing - review& editing.
A. Persdotter: scanning electron microscopy experiments.
N. Abdou: NMR experiments, Writing - review& editing.
S. Xiong: conceptualization, supervision, review.
P. Johansson, F. Liu, A. Martinelli, L. Evenäs: writing - review& editing, funding acquisition, supervision.
A. Matic: conceptualization, funding acquisition, resources, supervision, validation, writing - review& editing.

Paper II:
Q. Wu: conceptualization, investigation, methodology, data curation, visualization, writing - original draft, writing - review& editing.
A. Persdotter: scanning electron microscopy experiments.
J. Jamroz: experiments.
A. Matic: conceptualization, funding acquisition, resources, supervision, validation, writing - review& editing.

Paper III:
Q. Wu, E. Esping, M. Afiandika: writing - original draft, writing - review& editing.
A. Matic and S. Xiong: conceptualization, funding acquisition, resources, supervision, validation, writing - review& editing.

Publications Not Included in This Thesis

1. **Q. Wu**, S. Xiong, F. Li, A. Matic, "Electro-Chemo-Mechanical Failure Mechanisms of Solid-State Electrolytes" *Batter. Supercaps* **2023**, *6*, e202300321.

2. N. Abdou, **Q. Wu**, L. Evenäs, A. Martinelli, A. Matic, "Influence of TFSI/FSI Anion Mixing on the Transport Properties in Pyrrolidinium-based Ionic Liquid Electrolytes" (In manuscript, N. Abdou and Q. Wu contribute equally to this work)

Contents

1 Introduction

The rapid diversification of energy-storage applications has created a growing need for batteries that can operate also under extreme environmental conditions. Beyond conventional consumer electronics and electric vehicles, emerging fields such as space exploration, oil and gas drilling, geothermal monitoring, aerospace power systems, and energy storage in tropical or desert regions require electrochemical systems capable of withstanding prolonged exposure to elevated temperatures (60-150 °C)[1,2]. Consequently, developing high-temperature batteries has become an important research focus. However, a high temperature introduces significant challenges. Conventional organic electrolytes suffer from poor thermal stability and high flammability, leading to accelerated solvent decomposition, gas evolution, and risks of thermal runaway. Elevated temperature also accelerates side reactions and degradation of interphases. These processes increase cell resistance, decrease Coulombic efficiency, and severely limit cycle life[3]. Addressing these issues requires electrolyte designs with enhanced thermal stability, suppressed flammability, and improved interfacial robustness.

Within this context, lithium-metal batteries (LMBs) are an attractive platform for high-temperature applications because Li metal offers the highest known theoretical capacity (3860 mAh g^{-1}) and the lowest electrochemical potential (–3.04 V vs. standard hydrogen electrode), enabling unprecedented energy density[4]. These advantages make LMBs well-suited for mission-critical systems where compact size, low mass, and long service lifetime are essential. However, practical deployment of LMBs is hindered by inhomogeneous Li deposition, dendrite growth, side reactions at the Li metal/electrolyte interface, and rapid interfacial degradation, which compromise Coulombic efficiency, capacity retention, safety, and cycle life[5].

The inhomogeneous deposition of Li originates from two coupled factors: transport limitations and interfacial reactions, forming the solid electrolyte interphase (SEI)[6,7], as well as interfacial kinetics, such as Li^+ desolvation at the electrode surface[8–10]. Therefore, electrolyte engineering by manipulating the solvation shell and the SEI properties, is a potential way to improve the performance of LMBs[11–13].

Ionic liquids (ILs) are molten salts at ambient temperature, with low vapor pressure, high thermal stability, and high ionic conductivity, effectively eliminating the flammability of electrolyte and thermal runaway at high temperature[14]. For Li ion electrolytes, a Li salt can be dissolved in an IL, offering a potential solution for safe high-temperature LMBs[15,16]. However, in IL electrolytes, the strong coordination between Li^+ and anions brings about a high desolvation energy barrier[17,18], slowing down Li^+ transfer kinetics, which is detrimental to the rate performance, and can promote the growth of Li dendrites[19,20]. How to manipulate the solvation structure of Li^+ in IL electrolytes to improve Li^+ transport kinetics without sacrificing Li^+ mobility and electrolyte safety is still a knowledge gap. Another route to use ILs is as additives in traditional electrolytes[21,22]. The ions from the IL can modify the solvation structure of Li^+ and ion distribution at the electrolyte/electrode interface.

This thesis aims to explore strategies to suppress Li dendrite formation, accelerate Li^+ transfer kinetics, and improve interfacial stability for safe, high-performance, and long-life high-temperature LMBs by electrolyte engineering. The main principles are to manipulate the solvation structure and ionic transfer limitations, electric double layer (EDL) structure, and the properties of SEI. Understanding the interplay between these factors and the structure-effect relationship between the deposition mechanism and the performance of high-temperature LMBs is the goal of the thesis.

In the thesis, two electrolyte-engineering strategies are presented. The first strategy focuses on manipulating the solvation structure of Li^+ in a dual-anion IL electrolyte (DAIL:LiTFSI/Pyr_{14}FSI = 1:4) by introducing $LiNO_3$ and sulfolane (SL). The coordination of Li^+-NO_3^-/SL competes with Li^+-FSI/TFSI coordination, weakening Li^+-anion interaction, reducing the desolvation barrier[23,24], and improving ion transfer and interfacial uniformity[25]. The resulting electrolyte (NS-DAIL) enables faster Li^+ transfer kinetics and more stable Li plating/stripping at elevated temperatures (Paper I).

The second strategy introduces the ionic liquid Pyr_{14}FSI as an additive to a benchmark carbonate electrolyte (LP30) to regulate the electrode-electrolyte interface. The addition of IL modifies Li^+ solvation, reorganizes the EDL, and modifies SEI[10,26]. This interfacial reconstruction delays the cationic depletion at the electrolyte/electrode interface during plating, enabling compact and reversible Li deposition even under high-temperature conditions (Paper II).

Finally, a review study summarizes the electro-chemo-mechanical coupling governing Li plating in LMBs, emphasizing how solvation structure, electrochemical parameters, mechanics, and SEI properties jointly determine plating/stripping behavior of Li-metal anodes (Paper III).

2 Lithium-metal batteries

LMBs are widely regarded as next-generation electrochemical energy storage systems owing to the low redox potential of Li-metal (–3.04 V vs. standard hydrogen electrode) and its high theoretical capacity (3860 mAh g^{-1}), enabling high energy density cells[27]. These properties can allow for LMBs with gravimetric energy density exceeding 500-600 Wh kg^{-1}, when paired with high-voltage cathodes, such as $LiNi_{0.8}Co_{0.1}Mn_{0.1}O_2$ (NCM811), or high-capacity sulfur or oxygen cathodes[28]. In volumetric terms, optimized Li-metal cells could surpass 1000 Wh L^{-1}, enabling longer driving ranges in electric vehicles and lighter power sources for aerospace, etc[29–31]. Thus, rechargeable LMBs have been called the "Holy Grail" of energy storage systems and have been investigated extensively during the last 40 years[32].

Extending the operation of LMBs to high temperature (high-temperature is typically ≥60°C) enhances ionic conductivity and accelerates electrode kinetics, giving rise to increased rate performance. The applicability at elevated-temperature environments also broadens their potential application in power converter halls, tropical areas, or electrified transportation exposed to harsh climates, e.g., space[33]. However, a major challenge for high-temperature LMBs is the thickening and degradation of interfacial layers, such as the SEI and cathode electrode interphase (CEI)[7,34]. High temperature also promotes electrode decomposition, producing volatile gases and reactive species that increase safety risks, such as swelling or thermal runaway[2]. Elevated temperatures also exacerbate parasitic reactions between the Li-metal anode and the electrolyte, accelerating electrolyte decomposition and continuous SEI growth, and depleting the limited Li inventory in the cell[35]. Moreover, the SEI can also dissolve or decompose at high temperature, causing loss of passivation and rapid electrode failure[2].

The thermal instability and flammability of traditionally used electrolytes based on organic solvents result in electrolyte decomposition and thermal runaway at high temperatures, posing safety risks for high-temperature LMBs[3,36].To mitigate these issues, strategies include replacing thermally unstable Li salts with thermally robust salts, introducing salt stabilizers or film-forming additives to construct heat-resistant SEI layers, and employing acid or water scavengers to suppress parasitic interfacial reactions and enhance high-temperature stability[2]. Ionic liquid electrolytes with high thermal stability are also promising candidates for the high-temperature LMBs[37].

2.1 Lithium-metal anodes

Unlike insertion-type anodes (e.g., graphite), Li metal functions as a hostless conversion anode, where Li^+ ions are directly reduced and deposited onto the Li surface during plating and are oxidized and dissolved back into the electrolyte during stripping. Owing to the absence of a structural host matrix to accommodate Li^+ insertion, the Li-metal anode experiences large volume changes during cycling, far exceeding those of intercalation anodes such as graphite (~10%) or silicon (~400%)[38–40]. The problem is further aggravated by dendritic and porous Li growth, which amplifies volumetric expansion and contraction.

In addition, Li-metal anodes face severe challenges from their high reactivity, poor reversibility, and uneven plating/stripping, leading to Li and electrolyte consumption. Reducing Li excess in LMB cells leads to the ultimate anode-free lithium-metal battery design, where a bare current collector (often Cu) serves as the initial Li deposition substrate[41]. This design offers maximum energy density but suffers from low Coulombic efficiency and short cycle life due to a high nucleation overpotential, dendritic Li growth, and unstable SEI formation. Continuous side reactions consume Li^+ and thicken the SEI, impeding ion transport through SEI[41]. To overcome these issues, two main strategies are pursued: 1) electrolyte engineering to tailor solvation chemistry, facilitate uniform SEI formation, and stabilize Li deposition[5]; and 2) current collector modification, enhancing lithiophilicity through surface coatings, heteroatom doping, or 3D structured architectures[42]. Together, these approaches aim to realize thin, robust, and ionically conductive interphases, enabling stable and high-efficiency operation of next-generation anode-free LMBs[43].

The electrochemical potential of Li is –3.04 V vs. standard hydrogen electrode, a double-edged sword. On the one hand, low potential is a prerequisite for obtaining a high cell voltage and energy density. On the other hand, the low potential is outside the electrochemical stability window of most electrolyte formulations, leading to side reactions between Li and the electrolyte during plating. Ideally, this results in the formation of a passivation layer, the SEI, which can stabilize the electrode/electrolyte interface[44]. During plating, Li ions need to be transported through the SEI and then plate beneath it. Hence, the nature of the SEI has a substantial influence on the plating behavior.

The failure of Li-metal anodes originates mainly from (Figure 2.1): 1) inhomogeneous Li deposition, where preferential deposition on surface protrusions drives the evolution of formation of porous structures and dendrites[45]. Dendritic structures not only risk short-circuiting the cell but can also fragment, generating electrically isolated metallic residues, commonly referred to as “dead” Li, which irreversible consume active Li and reduce coulombic efficiency[46]. 2) Continuous side reactions between the highly reactive Li metal and the electrolyte. This results in a dynamically reforming, or growth of the SEI that depletes the Li inventory, leading to irreversible Li loss and capacity fading[47]. A continuous thickening of the SEI increases the resistance, resulting in higher cell impedance and polarization, which leads to the energy being lost as heat rather than stored, and limited Li^+ transport through the SEI, causing sluggish electrochemical reactions and poor rate capability[48,49]. This fragile interphase further exacerbates inhomogeneous current distribution, accelerates dendrite growth, and amplifies electrolyte consumption[50,51]. 3) Large volume expansion and contraction during charge and discharge lead to mechanical stress, interfacial fracture, and instability of the SEI.

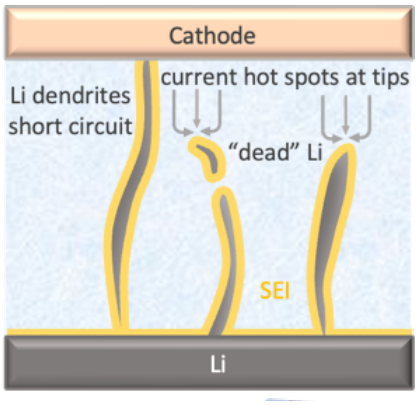

Figure 2.1. Schematic of failure mechanisms of Li-metal anode, including the formation of Li dendrites, inactive Li, and the continuous formation of SEI.[52] (From Paper III) (Reproduced from Ref. 49 with open access from Elsevier)

2.1.1 Li plating and stripping

Li plating is a multistage interfacial process strongly influenced by electrolyte formulation, overpotential, current density, and external parameters such as temperature, pressure, and substrate properties[52–54]. A SEI can form immediately upon contact between Li metal and electrolyte due to spontaneous reactions, which is the chemically formed SEI. SEI can also be electrochemically formed during the initial cycles as a result of electrolyte reduction until the interface is completely passivated. Parallel to SEI formation, an electric double layer is also formed at the Li/electrolyte interface, driven by electrostatic forces[55,56].

During charging of a Li-metal anode, solvated Li-ions migrate across the bulk electrolyte toward the anode under the applied electric field[57,58]. Approaching the Li surface, Li^+ undergoes desolvation driven by the electrostatic force from the negatively charged anode, which requires breaking of solvent, or anion, coordination[59,60]. The energy required for desolvation is linked to the strength and structure of the solvation shell of Li^+, and this step is widely recognized as a kinetic bottleneck[61]. At elevated temperature, the solvent exchange dynamic is accelerated, but increased temperature also amplifies parasitic reduction reactions.

The process of Li plating is a combination of mass transport in the electrolyte and interfacial charge transfer[62]. The formation of metal nuclei with a critical radius (r) on an electrode surface requires reduced metal ions to overcome an energy barrier for nucleation, which is governed by the degree of electrochemical supersaturation at the interface[62]. This supersaturation is experimentally reflected by the overpotential, serving as the measurable driving force for nucleation. The total nucleation overpotential can be deconvoluted into three contributions: charge-transfer, diffusion, and interfacial overpotentials. An additional barrier arises from ion transport through the SEI, which further influences nucleation kinetics[63].

To have a clear understanding of nucleation and deconvolute each of these overpotential contributions from the voltage response, a schematic of nucleation and the voltage-time profile under galvanostatic conditions is shown in Figure 2.2. When applying a current,

an initial voltage drop is observed (Figure 2.2 b), corresponding primarily to SEI formation. Simultaneously, solvated Li^+ is transported in the bulk electrolyte and arrives at the surface of the Li-metal anode, and Li^+ undergoes desolvation driven by the electric field (Figure 2.2a). After the desolvation, Li^+ is reduced to metallic Li and adsorbs on the substrate surface and forms adatoms, which is a charge transfer process. This corresponds to the peak in the voltage-time profile, representing Li nucleation. The magnitude of the nucleation peak corresponds to the nucleation overpotential (η_n), reflecting the total energy barrier for Li nucleation, which includes desolvation, charge transfer (reduction), and interfacial formation energies[63].

Finally, a gradual voltage rise transitioning into a plateau reflects the post-nucleation growth stage (Figure 2.2 b). Here, the overpotential minimum (η_m) marks the shift from charge-transfer-controlled to mass-transport-limited behavior, while the plateau after the overpotential minimum is attributed to a combination of bulk diffusion overpotential and SEI surface diffusion overpotential[64]. (Figure 2.2 a) The growth can proceed via lateral spreading or tip growth, depending on local ion concentration, electric field amplification, substrate, and SEI properties[64].

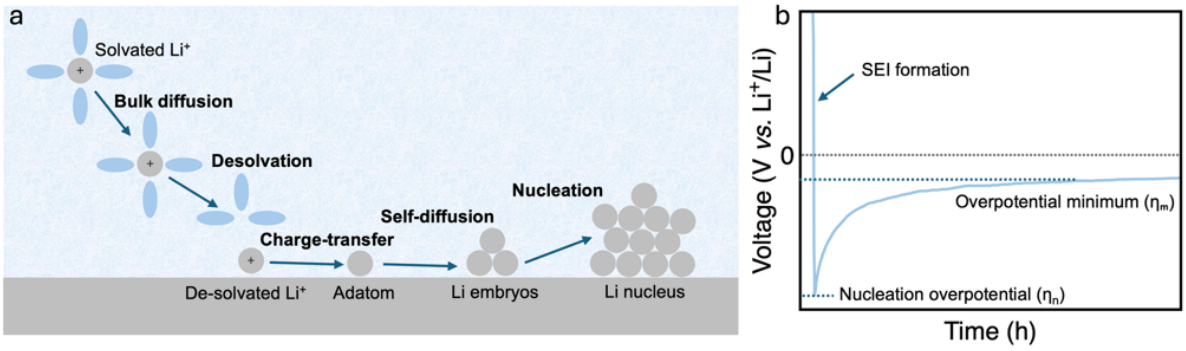

Figure 2.2. (a) Schematic of nucleation during Li plating.[64] (Reproduced from Ref. 61 with open access from Elsevier); (b) voltage-time profile in a galvanostatic plating experiment.

During plating, Li-ions are consumed at the interface and anions are expelled from the interface, driven by the electric field. This creates an ion concentration gradient in the electrolyte near the electrode surface, which is counteracted by diffusion[8,65]. For currents greater than the diffusion limit, the ion concentration at the electrode surface becomes zero after a given time, and the electrolyte turns to a dielectric fluid, causing inhomogeneous Li plating[66]. The characteristic time scale for this process is known as the "Sand's time" (τ_s)[9]. At $t > \tau_s$, Li plating will preferentially occur on surface protrusions where the ion concentration is higher, resulting in dendritic growth[9]. (Figure 2.3)

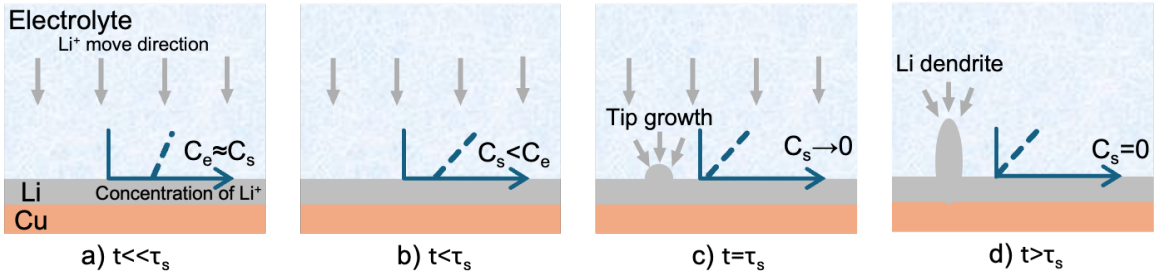

Figure 2.3. Schematic of Li dendrite formation based on transport-limitations (C_s and C_e represent Li^+ concentration at electrode/electrolyte surface and in bulk electrolyte, respectively), (a) $t<<\tau_s$ (τ_s is Sand's time): Li deposition starts and can be homogeneous; (b) $t< \tau_s$: Li^+ ion concentration gradient (dashed line) develops; (c) $t=\tau_s$: time when the Li^+ concentration at the Li-electrolyte interface approaches zero; and (d) $t> \tau_s$: after Sand's time is reached, Li dendrites form.

Bai et al. studied the different formation mechanisms of mossy and dendritic Li by observing the growth process in a glass capillary cell[67]. They found that mossy Li growth is a reaction-limited process, while dendritic Li growth is transport-limited. As shown in Figure 2.4 a, at a constant current density, mossy Li tends to grow from the root at the beginning of plating. With continued Li plating, the salt concentration near the substrate surface decreases, and with ion depletion, dendritic Li suddenly shoots out, which is evidence of tip growth. The Sand's time was experimentally determined via this visualization of Li plating, and an apparent diffusion coefficient of Li^+ could be calculated. The limiting current density was derived as $J_{lim} = 2z_c c_0 F D_{app}(t_a L)^{-1}$, where z_c is the charge of the cation, c_0 is the bulk salt concentration, F is Faraday's constant, D_{app} is the apparent diffusion coefficient of Li^+, t_a is the transference number of anions, and L is the distance between the electrodes[67]. If the current density $J < J_{lim}L$, no tip-growth will occur; if $J > J_{lim}L$, tip-growth will occur within the Sand's time. Based on this formula, an electrolyte with a high salt concentration and a low anion transference number is desirable, since it results in a longer Sand's time. For instance, in the electrolyte 1 M $LiPF_6$ in ethylene carbonate (EC) and dimethyl carbonate (DMC) (volume ratio of 1:1), when the distance between the two electrodes is 5 mm, and the calculated D_{app} from experimental result is ~ 1.0×10^{-6} cm^2 s^{-1}, the J_{lim} was calculated to be ~ 1 mA cm^{-2}, which was consistent with experimental observation. Bai et al. also defined a Sand's capacity (C_s) based on Sand's time theory, $C_s = J\tau_s$, as shown in Figure 2.4 b, which provides a simple design constraint to avoid dendritic Li growth[67].

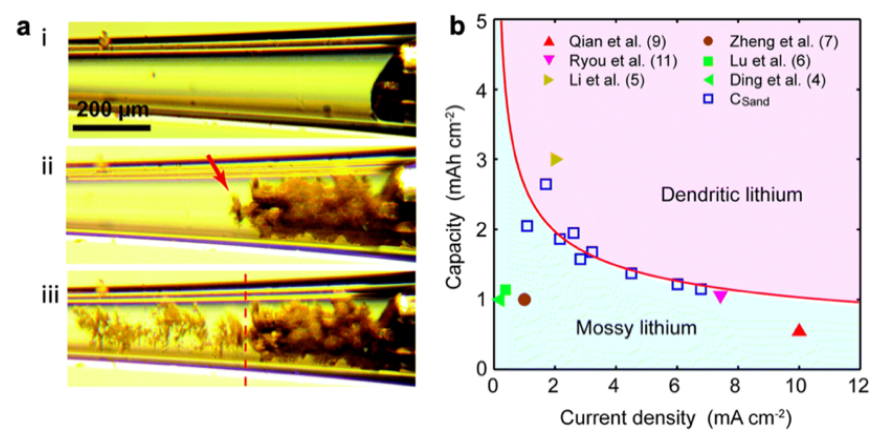

Figure 2.4. (a) In situ optical microscopy images of the growth of Li during electroplating with the increase of time. Red arrow in (ii) points to the emergence of dendritic Li. Red dashed line in (iii) labels the morphological difference between the pre- and post-Sand's time Li plating; (b) Sand's capacity versus current density.[67] (Reproduced from Ref. 64 with open access from Royal Society of Chemistry)

2.1.2 Solid electrolyte interphase

The electrochemical potential of Li (–3.04 V vs. standard hydrogen electrode), is outside the electrochemical stability window of most common electrolyte formulations. This leads electrochemical reduction of the electrolyte during plating. Ideally, this results in the formation of a passivation layer, the SEI, which can stabilize the electrode/electrolyte interface[7]. Thus, the SEI should form during the initial cycles until the Li metal anode is completely passivated[6].

During plating, the desolvated Li^+ ions need to be transported through the SEI and then plate beneath it. Hence, the nature of the SEI has a substantial influence on the plating behavior. (Figure 2.5) Most important properties of the SEI for homogeneous Li plating are[68]:

1) mechanical strength: the SEI needs to have a Young's modulus of 4.0 GPa and an elastic modulus of 3.0 GPa to accommodate volume expansion and avoid the cracking of the SEI during Li plating[48];

2) chemical composition: an SEI composed mainly of inorganic compounds, such as LiF, has higher ionic conductivity and mechanical strength, mitigating stress concentration after Li plating;

3) electronic conductivity: a SEI with high electronic conductivity leads to poor passivation of the interface due to continuous reduction of the electrolyte, leading to the growth of the SEI with cycling;

4) ionic conductivity: a SEI with high ionic conductivity facilitates uniform Li^+ transport across the interface, enabling homogeneous charge distribution during electrodeposition. In contrast, a poorly conductive SEI brings about Li^+ depletion in SEI[48];

5) uniformity: a chemical nonuniform SEI leads to heterogeneous ionic conductivities, and increased ion transport in domains with high conductivity leads to the formation of hot spots and nonuniform Li plating;

6) morphology: dense SEI mitigates side reactions between the electrolyte and the Li electrode.

The ideal SEI should therefore be thin, dense, mechanically robust, conductive to Li ions, and insulating to electrons, so it is important for these properties to be tunable to obtain uniform Li plating[44,69,70]. SEI properties are, to a large extent, determined by the electrolyte composition. Hence, electrolyte engineering is an effective way to tune the nature of the SEI and battery performance.

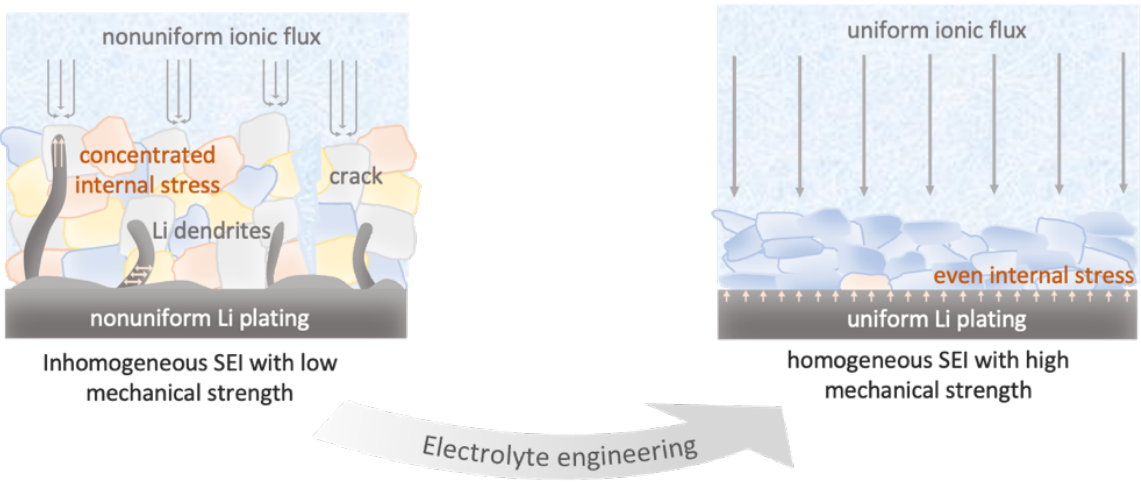

Figure 2.5. Schematic of the function of SEI formed on a Li metal anode.[52] Left: organic compound dominated and inhomogeneous SEI with low ionic conductivity, leading to Li^+ depletion and uneven deposition. Right: optimized inorganic-rich SEI with a homogenous structure and sufficient mechanical modulus leads to even Li plating, and homogenous internal stress distribution. (From Paper III) (Reproduced from Ref. 49 with open access from Elsevier)

2.1.3 Electric double layer

The electric double layer (EDL) at the anode/electrolyte interface influences ion transport, electrochemical reactions, and stability. Key considerations include the structure of the EDL, which is closely related to the electrolyte composition, ion transport in EDL, and the effect of potential and electrode surface conditions[71]. Understanding and optimizing the EDL can enhance battery performance, particularly in terms of Li deposition.

The formation of an EDL at the surface of a metal anode is driven by electrostatic interactions and the minimization of electrochemical potential differences at the interface between the Li metal anode and the electrolyte[72]. When a potential difference is applied across the cell during charging, Li^+ from the electrolyte migrate toward the negatively charged Li metal anode, while counterions (i.e. anions in the electrolyte) are repelled[73]. This results in a region of charge separation at the interface, where the electrode has a net negative charge and the electrolyte near the surface has an

accumulation of positive charges (Li^+)[74], with a compact layer of Li-ions at the interface (Helmholtz layer), followed by a diffuse layer of less tightly bound ions[75].

The redistribution of ions at the interface balances the potential drop across the solid-liquid interface. The accumulation of Li ions on the Li-metal electrode surface leads to a linear potential drop within the Helmholtz layer, (Figure 2.6 a) the layers of opposite polarity form at the interface between the electrode and electrolyte, resulting in a capacitive contribution[76]. A similar linear potential drop can also be caused by two layers of oppositely charged ions at the electrode. (Figure 2.6 b) In highly concentrated electrolytes, Li^+ is coordinated by multiple anions instead of just solvent molecules. The inner layer of the EDL is then composed of closely packed ions with few solvent molecules, so the EDL becomes much more compact compared to the situation in dilute electrolytes[77]. The diffuse layer is negligible because of the extreme ionic strength, leading to a combination of linearly and exponentially decreasing potentials within the double layer region, as illustrated in Figures 2.6 c and d.

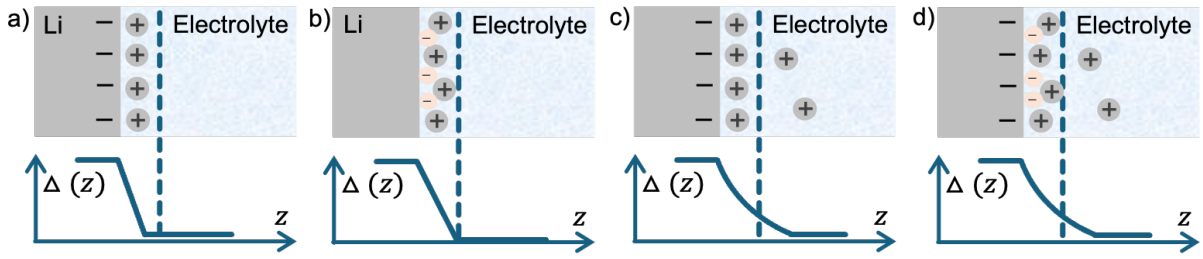

Figure 2.6. Illustration of possible scenarios for electric double layers. (a) Charged electrode covered by counter ions; (b) two layers of oppositely charged ions at uncharged electrode; (c) and (d) scenarios depicted in panels (a) and (b), respectively, with an additional diffuse layer of ions.

If Li^+ is solvated by solvent molecules in dilute electrolytes, more solvent molecules are involved in EDL, which might lead to a thicker and less-organized structure. For IL electrolytes, Li^+ is solvated by anions of the ionic liquid, sometimes forming contact ion pairs or aggregates. Near the electrode, IL cations and anions arrange in alternating layers due to strong Coulombic correlations. Thus, there is no real diffuse layer, but a layered structure[78].

The structure of EDL influences Li plating and stripping by affecting the Li^+ distribution at the electrode surface[58]. A well-structured EDL with compact and uniform Li^+ accumulation at the inner layer facilitates homogenous plating, reducing the risk of dendrite growth. In paper II, $Pyr_{14}FSI$ is introduced into the carbonate electrolyte LP30, which changes the ionic distribution in the EDL, where the bulky cations (Pyr_{14}^+) from the IL adsorb at the Li surface, delaying cation depletion at the interface, increasing the Sand's time, and suppressing growth of protrusions. (Figure 2.7)

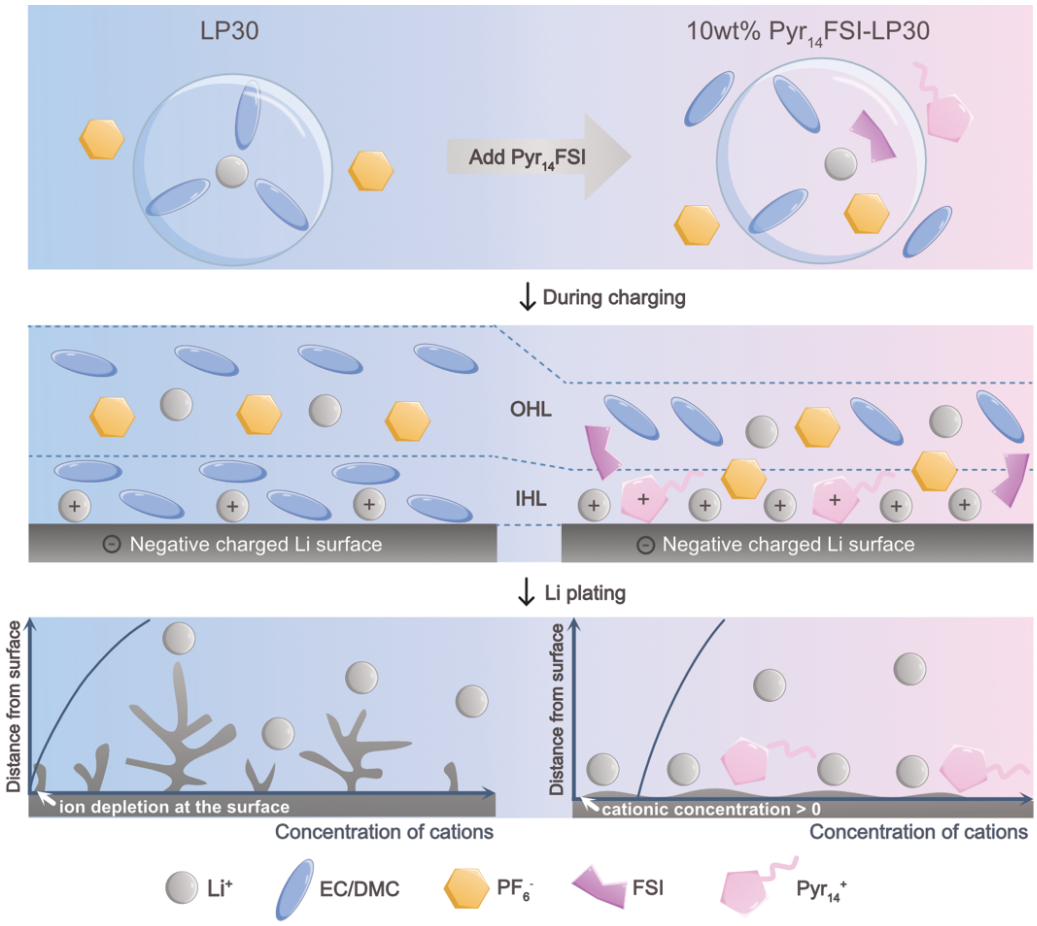

Figure 2.7. Schematic of the structure of EDL and its influence on Li plating morphology. Left: In LP30 electrolyte, the inner layer of EDL contains solvent molecules. During plating, the Li^+ at the electrode surface is depleted after a certain time, and Li^+ preferentially deposits on the tips where the Li^+ concentration is higher than at the surface. Right: In $Pyr_{14}FSI$-LP30 electrolyte, bulky cations (Pyr_{14}^+) from IL adsorb at the Li surface, and the Stern layer of EDL is dominated by cations. The depletion of cations at the surface is delayed, rendering a uniform Li plating.

The EDL and the SEI are closely interlinked at the Li electrode/electrolyte interface. The EDL defines the initial spatial distribution of ions and solvent molecules near the Li surface, determining which species are first reduced when electrochemical polarization begins. Thus, the composition of the EDL directly relates to SEI formation, which means an anion-rich EDL favors an inorganic SEI layer (LiF, Li_2O), while a solvent-dominated EDL produces an organic-rich SEI.

In conclusion, the overall deposition morphology of Li arises from the interplay between solvation structure (determining SEI chemistry), desolvation kinetics (governing charge-transfer barriers), EDL organization (regulating interfacial ion flux and affect the composition of SEI), SEI properties (controlling Li^+ transport and internal stress distribution), nucleation pathways (dictating growth modes), applied current density (electric field), and overpotential. These coupled processes ultimately dictate Coulombic efficiency, interfacial stability, and deposition morphology. (Figure 2.8)

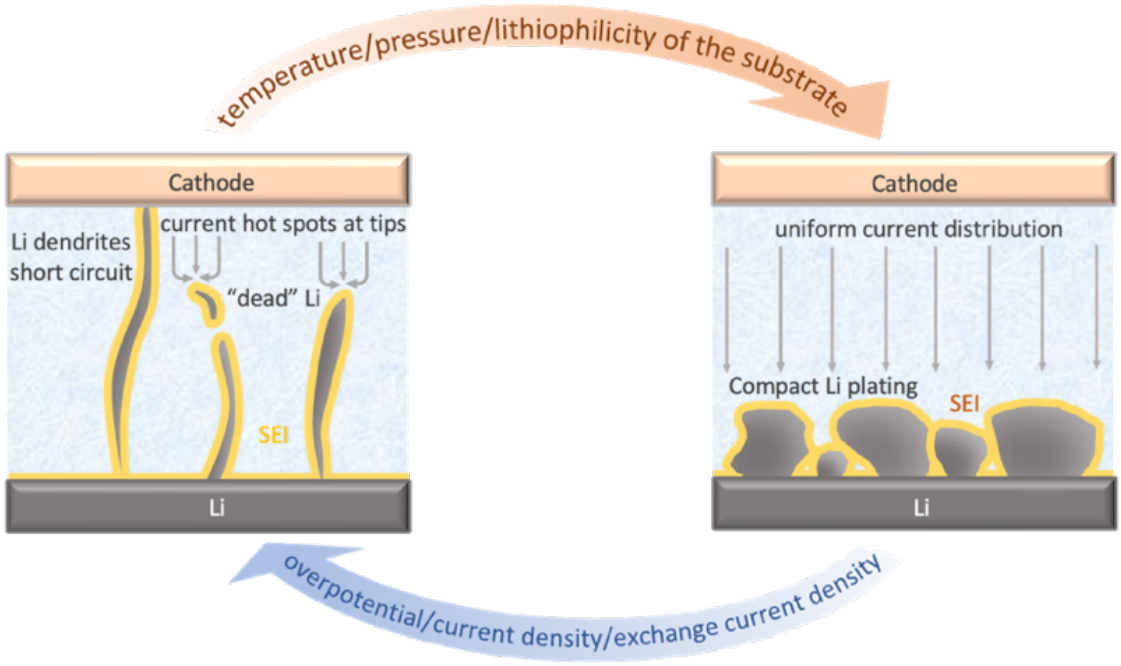

Figure 2.8. Schematic of the factors controlling Li growth[52] (From Paper III) (Reproduced from Ref. 49 with open access from Elsevier)

2.2 Electrolytes for Li-metal batteries

The electrolyte for LMBs, as for most batteries, typically consists of a lithium salt dissolved in one or more organic solvents, often with specific additives to improve stability. An ideal electrolyte must provide high ionic conductivity, a wide electrochemical stability window, and chemical compatibility with electrodes and cell components[32].

The solvent governs the solvation structure, and ion transport. A suitable solvent should exhibit a high dielectric constant for effective salt dissociation, low viscosity for high ion mobility, and chemical and electrochemical stability toward both the Li anode and high-voltage cathodes. Carbonate solvents such as ethylene carbonate (EC) and dimethyl carbonate (DMC) are widely adopted due to their high dielectric constants and ability to form a passivating SEI[79]. The lithium salt provides the ionic conductivity and influences the interfacial chemistry by solvation structure. Among various candidates, $LiPF_6$ is most common in carbonate-based systems because of its balanced solubility and interfacial reactivity. However, it is thermally unstable and tends to undergo hydrolysis, generating reactive species such as HF and PF_5, which accelerate electrolyte decomposition and damage electrode surfaces. This degradation becomes especially problematic at elevated temperatures, where these side reactions are amplified[80]. Alternative salts such as LiTFSI, LiFSI, and LiBOB offer improved thermal and chemical stability and are increasingly favored for high-temperature applications.

Elevated temperatures (≥60°C) significantly alter electrolyte behavior. While ionic conductivity increases due to enhanced ion mobility, electrochemical stability decreases as side reactions are accelerated. The SEI and CEI layers undergo continuous degradation and reconstruction, leading to thickening, increased interfacial resistance, and eventual loss of active Li in the electrolyte. Additionally, salt or solvent degradation

at high temperatures can release volatile or flammable products, posing safety risks. Therefore, the design of high-temperature electrolytes requires a careful balance between fast ion transport and interfacial/thermal robustness.

2.2.1 Ionic liquid electrolytes

Ionic liquids have attracted extensive attention as alternative electrolytes for high-temperature LMBs owing to their negligible volatility, nonflammability, wide electrochemical stability window, and outstanding thermal stability[2,81,82]. Their bulky, weakly coordinating cations and highly charge-delocalized anions result in fundamentally different solvation environments compared to organic-solvent-based electrolytes, with no solvent participation in Li^+ coordination and favoring inorganic-rich SEI formation[83,84]. This suppresses parasitic side reactions, and enhances mechanical robustness of the SEI. Nevertheless, a high viscosity and sluggish Li-ion transport cause uneven Li-potential distribution at the interface, giving rise to nonuniform Li plating/stripping and growth of Li dendrites[15].

Imidazolium- and pyrrolidinium-based ionic liquids have emerged as promising candidates for LMB electrolytes due to their high ionic conductivity, low viscosity, and wide electrochemical stability window[85,86]. These IL families enable efficient Li^+ intercalation into cathode materials, meeting key industrial requirements for practical energy storage systems. By pairing their cations with various anions, such as BF_4^-, PF_6^-, and TFSI, a wide range of ILs can be designed with optimized physicochemical and interfacial properties[37].

For instance, Peng et al. developed an IL-based electrolyte composed of 4.5 M LiFSI in $Py_{13}FSI$ with 1 wt% LiTFSI, which exhibited an electrochemical window exceeding 5 V and formed a stable, F-rich SEI on Li metal[87]. Liu et al. further advanced this concept by synthesizing a fluorinated pyrrolidinium cation, 1-methyl-1-propyl-3-fluoropyrrolidinium, coupled with the FSI anion (PMpyrfFSI) with both cationic and anionic fluorine sources. This IL features a unique fluorine-rich interfacial chemistry on both Li-metal and high-Ni cathodes[88].

In addition to directly using ILs as electrolytes, they are increasingly being applied as additives to conventional electrolytes to improve high-voltage and thermal stability[89]. Even at modest concentrations, IL additives can, on one hand, manipulate the solvation shell of Li^+ to an anion-rich structure, bringing more anion to the electrolyte/electrode surface and forming an inorganic-dominant SEI[90]. On the other hand, introducing IL additives with bulky cations and mobile anions can reorganize the EDL and delay ion depletion near the electrode surface, thereby suppressing dendrite formation[91]. Moreover, IL-derived SEIs, dominated by inorganic anion-reduction products, exhibit higher ionic conductivity than organic-dominated SEI[92]. This dual role of interfacial stabilization without compromising bulk conductivity positions IL additives as a versatile design strategy for enabling safe, dendrite-free, and thermally robust high-temperature LMBs.

2.2.2 Solvation structure

In liquid electrolytes, the solvation structure describes the local coordination environment surrounding a cation (e.g., Li^+) formed through electrostatic and donor-acceptor interactions between ions and solvent molecules and/or anions, and governs ion transport, interfacial reactions, and SEI chemistry[93]. The nature and strength of Li^+-solvent and Li^+-anion interaction dictate desolvation barriers at the electrode surface, the reduction pathways of electrolyte components, and thereby the composition and mechanical properties of the SEI. Changes in solvation, such as shifting from solvent-dominated to anion-rich coordination, can drastically alter interfacial kinetics, Li^+ conductivity in bulk electrolyte, desolvation kinetics, and Li deposition morphology[25,94].

Fundamentally, the formation of a solvation shell can be understood through Lewis acid-base theory, where Li^+ is a strong Lewis acid with high charge density. It preferentially coordinates with hard Lewis bases, typically the electron-rich atoms (O, N, F) in solvents or anions. The strength of these interactions depends on the donor number (DN) of the coordinating species (a measure of electron-donating ability) and the acceptor number (AN) of the cation[95].

Each Li^+ ion is typically surrounded by a primary solvation shell, composed of several coordinating molecules or anions. The balance between cation-solvent, cation-anion, and solvent-solvent interactions defines the composition and geometry of this shell[94]. When the solvent's Lewis basicity or dielectric constant is high, solvent-separated ion pairs (SSIPs) dominate, where Li^+ and the counter-anion are screened by solvent molecules. Conversely, in weakly solvating or concentrated electrolytes, contact ion pairs (CIPs) or aggregated ion clusters (AGGs) form as anions penetrate the primary coordination sphere[90,96].

This structural hierarchy is dynamic and responsive to local electric fields, temperature, and salt concentration in the electrolyte. The exchange rate of coordinating species determines desolvation kinetics, which critically influences interfacial charge transfer and SEI formation[93]. A stronger Li^+-solvent or Li^+-anion interaction enhances solvation stability but raises the desolvation energy barrier, slowing down interfacial kinetics. Conversely, a weaker, more labile coordination accelerates desolvation but may compromise electrochemical stability[25,94]. Solvent-dominated coordination typically lowers viscosity and enables high ionic conductivity but promotes solvent decomposition and organic-rich SEI, whereas anion-rich solvation favors inorganic-rich, mechanically robust SEI[92,97]. Rational manipulation of solvation structure has therefore emerged as a powerful design principle for electrolytes. Strategies include highly concentrated electrolytes to enforce anion participation[98], localized highly concentrated formulations with inert diluents to balance increased viscosity, incorporation of fluorinated solvents to weaken Li^+-solvent interactions[99–101], and to promote anion-rich coordination[91]. Additives or ILs (with bulky, weakly coordinating cations and delocalized anions) can further modulate the solvation structure, creating anion-rich solvation shells that promote inorganic SEI formation[91].

Different from organic solvent-based electrolytes, anions dominate the solvation structure of Li^+ in IL electrolytes, bringing about a high desolvation energy because of the high charge density of Li^+ ions (strong Lewis acid), highly delocalized charges of anions, and the absence of Li^+-solvent-coordination competition[17]. This slows down Li^+ transfer kinetics, which is detrimental to the rate performance.

However, given that IL electrolytes are organic solvent-free, simply increasing the concentration of Li salt is not a viable strategy to tune the solvation structure because the viscosity will increase dramatically, and Li^+ mobility will drop due to the "overcrowded ionic environment" in IL electrolytes. Introducing excess solvent to dilute IL electrolytes reduces thermal stability. How to manipulate the solvation structure of Li^+ of IL electrolytes for improving Li^+ transport kinetics without sacrificing Li^+ mobility and safety is still a knowledge gap. Based on this, a specific method for locally manipulating the Li^+-anion coordination of ILE was proposed by us, which involves introducing additives with a high donor number[12,95] into IL electrolytes (Paper I). The competition between the coordination of Li^+ to species with high donor number or to anions weakens the overall Li^+ coordinated environment, lowering the desolvation energy barrier and ensuring facile Li^+ ion transport and good rate performance.

In Paper I, lithium nitrate ($LiNO_3$) and sulfolane (SL) with higher donor number will be introduced into a dual-anion IL electrolyte (DAIL: LiTFSI/Pyr_{14}FSI with molar ratio of 1:4 (Lithium bis(trifluoromethanesulfonyl)imide/1-butyl-1-methylpyrrolidinium (fluorosulfonyl)imide)) to locally manipulate the Li-anion coordination environment. The stronger coordination of Li^+ to NO_3^-/sulfolane[102–104] competes with the coordination of Li^+ to FSI/TFSI[105] of the ionic liquid electrolytes[23,24]. (Figure 2.9)

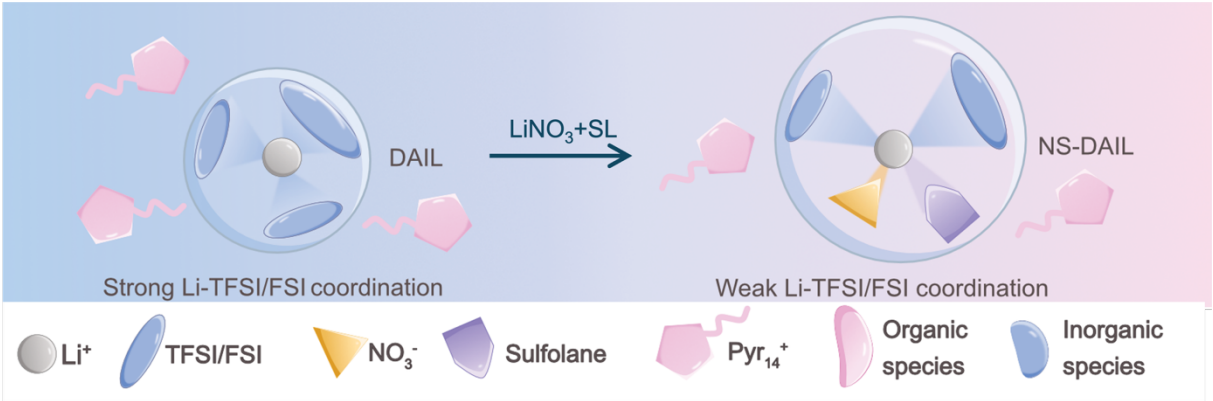

Figure 2.9. Schematic of manipulation of Li^+-anion coordination of IL electrolyte.

2.2.3 Electrolyte engineering

For traditional commercial electrolytes with carbonate solvents (for example, propylene carbonate (PC)), Li ions coordinate primarily with organic molecules due to the high polarity of carbonates[106], inducing a fragile, organic-rich SEI with high ionic diffusion barriers, leading to ion depletion and dendritic growth[107].

Substitution of ester-based solvents with ether-based solvents, that have weak polarity and more resistance to reduction, decreases the proportion of organic molecules in the solvation shell and leads to a thinner, inorganic-rich SEI, which facilitates uniform Li

plating and higher CE. The formation of flexible oligomers in the SEI due to the application of ether-based electrolytes also improves the SEI's stability and flexibility[108].

Introducing additives is also a useful strategy to improve the SEI. Fluoroethylene carbonates (FEC) are fluorinated additives that produce a LiF-rich SEI and a low ionic diffusion barrier[109]. Vinylene carbonate (VC) is easily polymerized on the Li surface, leading to the formation of long-chain hydrocarbon components, which is advantageous for creating a flexible and stable SEI[12,107]. Electrolytes with lithium bis(oxalato)borate (LiBOB) as an additive help promote even Li plating by forming fibrous Li surfaces instead of dendritic Li growth[110]. Lithium difluoro(oxalate)borate (LiDFOB) can also improve the thermal stability of the electrolyte and form a stable SEI[111]. Textured and uniform Li plating with spherical Li particles was obtained by adding $LiNO_3$ to an ether-based electrolyte[112]. The addition of $LiNO_3$ also leads to the formation of Li_3N in the SEI, which is favorable for improving ionic conductivity[113].

Highly concentrated electrolytes have been considered an effective route to obtain homogeneous Li plating[98]. The high salt concentration leads to more anions participating in the solvation structure, forming inorganic-rich SEIs; this not only increases the Li^+ conductivity but also suppresses diffusion-limited Li dendrite growth and yields a high CE[98]. However, concentrated electrolytes have high viscosity and density, which decrease the LMB's electrochemical performance. Introducing weakly polar solvents, such as bis(2,2,2-trifluoroethyl) ether (BTFE), as diluents to form localized high concentration electrolytes reduces the viscosity but preserves the anion-rich solvation structure[99,100]. Lee et al. observed the Li plating morphology by cryo-focused ion beam (cryo-FIB) in a conventional ester-based electrolyte (1.0 M LiPF6 EC/EMC 3:7 (Gen II)), in a single salt highly concentrated electrolyte (4.6 M LiFSI-DME (SSEE)), and in a bisalt highly concentrated electrolyte (4.6 M LiFSI + 2.3 M LiTFSI in DME (BSEE))[114].

3 Experimental methods

3.1 Materials preparation

3.1.1 Electrolytes

The Li salts lithium bis(trifluoromethylsulfonyl)imide (LiTFSI) (99.9%), and Lithium bis(fluorosulfonyl)imide (LiFSI) (99.9%), the ionic liquids 1-Butyl-1-methylpyrrolidinium bis(fluorosulfonyl)imide ($Pyr_{14}FSI$) (99.9%), and 1-Butyl-1-methylpyrrolidinium bis(trifluoromethylsulfonyl)imide ($Pyr_{14}TFSI$) (99.9%), sulfolane (SL) (99%), and the standard electrolyte 1 M $LiPF_6$ in EC: DMC (v:v, 50:50) (LP30) were all purchased from Solvionic. Lithium nitrate ($LiNO_3$) (99.9%) was purchased from Sigma Aldrich.

LiTFSI, LiFSI, $Pyr_{14}FSI$, $Pyr_{14}TFSI$, and $LiNO_3$ were vacuum-dried in a Büchi oven at 80 ºC for 12 hours before preparation of electrolytes. LiTFSI was dissolved in $Pyr_{14}FSI$ at a molar ratio of 1:4, and stirred to obtain the dual anion ionic liquid electrolyte (DAIL). $LiNO_3$ was dissolved in SL at a molar ratio of 1:4, and stirred to obtain Solution 1 (solubility of $LiNO_3$ in SL is 2 mmol/g). 56.89 mg of Solution 1 was added into 2365 mg DAIL to obtain NS-DAIL electrolyte (molar ratio LiTFSI : $Pyr_{14}FSI$: SL : $LiNO_3$ = 16:64:4:1). 100 and 200 µl $Pyr_{14}FSI$ was dissolved in 1 ml LP30 to obtain 10wt% and 20wt% $Pyr_{14}FSI$-LP30. Single-FSI and TFSI-based IL electrolytes were prepared according to the molar ratio shown in the Tables 3.1 and 3.2.

Table 3.1. Composition of single FSI-based IL electrolytes.

Molar concentration	LiFSI	$Pyr_{14}FSI$	$LiNO_3$	Sulfolane
LiFSI-$Pyr_{14}FSI$	1	4	/	/
LiFSI-$Pyr_{14}FSI$-SL	4	16	/	1
LiFSI-$Pyr_{14}FSI$-SL-$LiNO_3$	16	64	1	4

Table 3.2. Composition of single TFSI-based IL electrolytes.

Molar concentration	LiTFSI	$Pyr_{14}TFSI$	$LiNO_3$	Sulfolane
LiTFSI-$Pyr_{14}TFSI$	1	4	/	/
LiTFSI-$Pyr_{14}TFSI$-SL	4	16	/	1
LiTFSI-$Pyr_{14}TFSI$-SL-$LiNO_3$	16	64	1	4

All the electrolytes were prepared and stored in an argon-filled glovebox with O_2 and H_2O levels <1 ppm.

3.1.2 Electrodes

Li foil was purchased from Honjo Metal (200 µm in thickness, 3.5 cm in width, purity >99.8%). Before use, the Li foil was brushed to remove the surface oxidized layer and punched into disks with a diameter of 11 mm.

Cu foil was purchased from Goodfellow, thickness 0.1 mm. The Cu foil was punched into disks with a diameter of 14 mm and washed with ethanol and subsequently dried for 2 h under vacuum at room temperature.

Lithium titanium oxide (LTO) cathode with capacity of 2 mAh cm^{-2} was purchased from Nanografi Nanotechnology.

Lithium iron phosphate (LFP) cathode with capacity of 1 mAh cm^{-2} was purchased from Sigma-Aldrich Sweden AB. LTO and LFP were punched into 10 mm disks.

3.1.3 Battery assembly

Coin cells (2032) were assembled with a top cap, gasket, cathode, separators, anode, spacer, spring, and bottom cap. Two layers of Solupor separator were used in the coin cell, and 70 µL of electrolyte was added to each coin cell. (Figure 3.1)

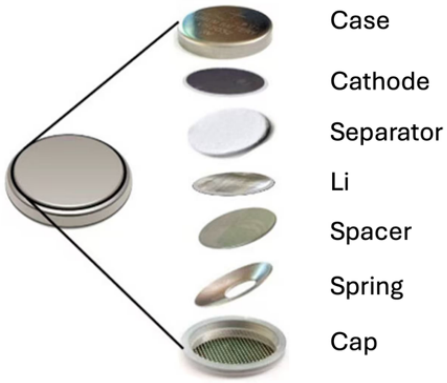

Figure 3.1. Configuration of coin cell.

Swagelok cells were used for preparing SEM samples to study deposition. The anode was Li-metal, with a diameter of 10 mm, and a Cu foil with a diameter of 10 mm was used as working electrode. A polypropylene spacer, thickness 2 mm, and outer diameter 10 mm with an inner hole with a diameter of 6 mm, was used to separate the two electrodes. (Figure 3.2)

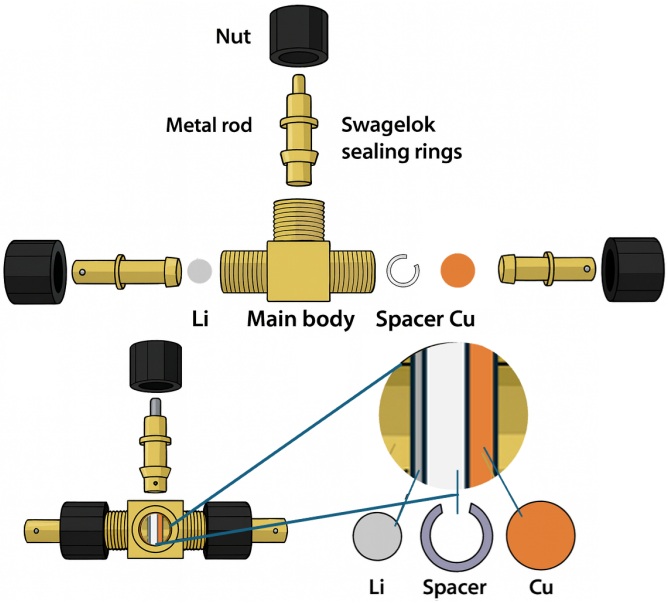

Figure 3.2. Configuration of Swagelok cell, used for deposition experiments on Cu for SEM investigation.

3.2 Physicochemical characterization

3.2.1 Raman Spectroscopy

Raman spectroscopy is a vibrational spectroscopic technique that provides molecular-level information about the structural and chemical characteristics of materials. It is based on the inelastic scattering of monochromatic light, known as Raman scattering, which occurs when incident photons interact with molecular vibrations, resulting in a small shift in the energy of the scattered photons. This energy shift corresponds to specific vibrational modes of the molecules, serving as a unique fingerprint of their chemical structure and interaction with the surrounding molecules/ions[115]. Here, we used Raman spectroscopy to study the solvation structure of electrolytes.

Raman spectroscopy was performed on a Bruker MultiRAM Fourier transform Raman spectrometer equipped with a Nd:YAG laser (1064 nm) and a liquid nitrogen-cooled Ge-diode detector. The nominal laser power was 720 mW, the resolution was set to 2 cm^{-1} (full width at half-maximum), the Blackman−Harris three-term window function was used for apodization, and spectra were obtained as the average over 1000 scans. Fitting of spectra was performed with OriginLab software, using a linear background and Voigt profiles.

The spectral region between 680-780 cm^{-1} in Raman spectra from the ionic liquid electrolyte DAIL and NS-DAIL was deconvoluted into components of solvation separated ion pairs (SSIP), contact ion pairs (CIP), and aggregate (AGG) of FSI (724, 733, and 748 cm^{-1}, respectively)[116], CIP of TFSI (747 cm^{-1}) and the two conformers of the free TFSI (cisoid and transoid, C1 at 739 cm^{-1} and C2 at 741 cm^{-1})[117]. An example of the fitting is shown in Figure 3.3. From the relative integrated intensities of the five components, we can estimate the population of free TFSI and TFSI coordinating to Li-ions, expressed as the fractions[118,119]:

$$C_{coord\,FSI} = \frac{A_{CIP}+A_{AGG}}{A_{SSIP}+A_{CIP}+A_{AGG}},\ C_{free\,FSI} = \frac{A_{SSIP}}{A_{SSIP}+A_{CIP}+A_{AGG}} \quad (1)$$

where A_{SSIP}, A_{CIP}, A_{AGG} are the integrated intensities of the bands SSIP, CIP, and AGG of FSI, respectively.

$$C_{coord\,TFSI} = \frac{A_{CIP}}{A_{SSIP}+A_{CIP}},\ C_{free\,TFSI} = \frac{A_{SSIP}}{A_{SSIP}+A_{CIP}} \quad (2)$$

where A_{SSIP} and A_{CIP} are the integrated intensities of the bands SSIP (two peaks), CIP of TFSI, respectively.

From the fractions of the free and Li-ion coordinated FSI/TFSI, Eqs. (1) and (2), the average number of FSI and TFSI around a Li-ion can be calculated as

$$N_{anion/Li} = \frac{C_{coord\ anion}}{x}$$

where x is the Li-ion concentration (molar fraction).

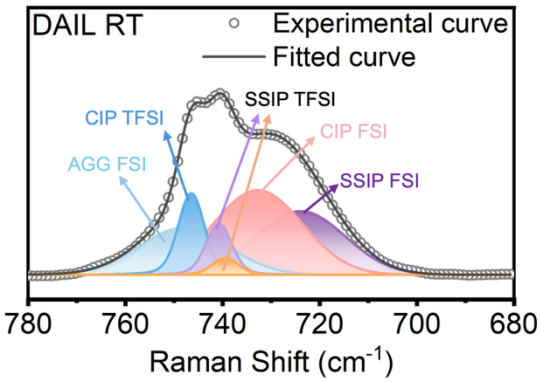

Figure 3.3. Raman spectrum of LiTFSI-$Pyr_{14}FSI$ (DAIL) electrolyte at room temperature in the range of 680-780 $cm^{-1}$and fit with six components.

The spectral region between 700-760 cm^{-1} in the Raman spectrum of LP30 and $Pyr_{14}FSI$-LP30 was deconvoluted into 6 bands (Figure 3.4), corresponding to the free EC-ring-bending vibration (I), EC coordinated to Li^+ (II), solvent separate ion pair (SSIP) of PF_6^- (III), contact ion pair (CIP) of PF_6^- (IV)[117], solvent separate ion pair (SSIP) of FSI (V), and contact ion pair (CIP) of FSI (VI) [116], respectively. The spectral region between 870-950 cm^{-1} in the Raman spectrum of LP30 and $Pyr_{14}FSI$-LP30 was deconvoluted into 4 bands (Figure 3.5), corresponding to free EC-ring-bending vibration (I), Li coordinated EC (II)[120], C-O stretching vibration of free DMC (III), Li coordinated DMC (IV) [117], respectively. The three peaks with low intensity correspond to a contribution from the ionic liquid cation Pyr_{14}. The fitting parameters of these three peaks were obtained from the fits to Raman spectra of the neat $Pyr_{14}FSI$ IL, which were used as references during fitting, and the intensity of these three peaks is standardized based on the added concentration of $Pyr_{14}FSI$.

An example of the fitting in the 700-760 cm^{-1} spectral region is shown in Figure 3.4. From the relative integrated intensities of the six components, we can estimate the population of free/Li coordinated EC, PF_6^-, and FSI, expressed as the fractions:

$$C_{coord\ EC} = \frac{A_{II}}{A_I + A_{II}},\ C_{free\ EC} = \frac{A_I}{A_I + A_{II}} \quad (1)$$

$$C_{coord\ PF_6^-} = \frac{A_{IV}}{A_{III} + A_{IV}},\ C_{free\ PF_6^-} = \frac{A_{III}}{A_{III} + A_{IV}} \quad (2)$$

$$C_{coord\ FSI} = \frac{A_{VI}}{A_V + A_{VI}},\ C_{free\ FSI} = \frac{A_V}{A_V + A_{VI}} \quad (3)$$

where A_I-A_{VI} are the integrated intensities of the bands I-VI, respectively.

An example of the fitting in the 870-950 cm^{-1} spectral region is shown in Figure 3.5. From the relative integrated intensities of the six components, we can estimate the population of free/Li coordinated DMC expressed as the fractions:

$$C_{coord\ DMC} = \frac{A_{IV}}{A_{III} + A_{IV}},\ C_{free\ DMC} = \frac{A_{III}}{A_{III} + A_{IV}} \quad (4)$$

From the fractions of the free and Li-ion coordinated EC/DMC/FSI/PF_6^-, Eqs. (1) (2) (3) (4), the average number of the EC/DMC/FSI/PF_6^- coordinating a Li-ion can be calculated as:

$$N_{Specie/Li} = \frac{C_{Specie}}{x}$$

where x is the Li-ion concentration (molar fraction).

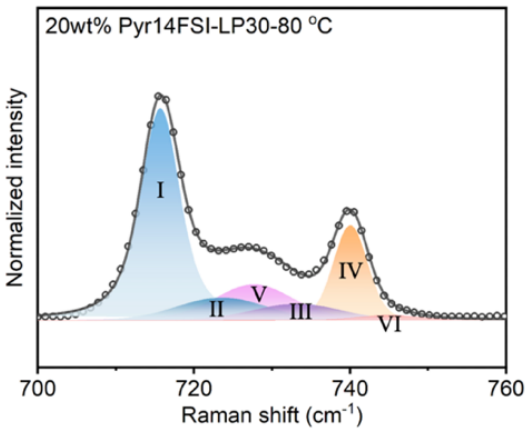

Figure 3.4. Raman spectrum of 20wt%Pyr_{14}FSI-LP30 electrolyte in the Raman shift range of 700-760 cm^{-1} and fitted result with six components.

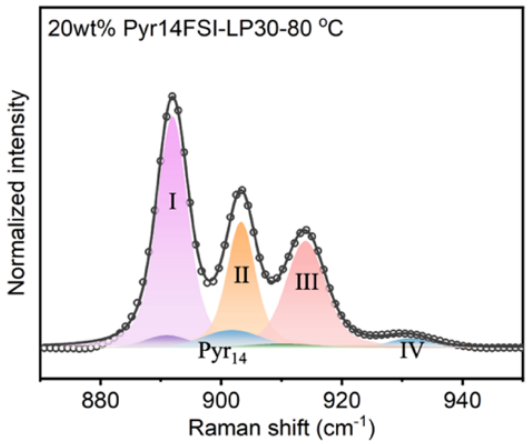

Figure 3.5. Raman spectrum of 20wt%Pyr_{14}FSI-LP30 electrolyte in the range of 870-950 cm^{-1} and fitted result with six bands and contributions for Pyr_{14}.

3.2.2 Differential Scanning Calorimetry

Differential Scanning Calorimetry (DSC) is used to investigate the thermal properties of materials by measuring the heat flow associated with temperature-dependent physical or chemical transitions. In a DSC experiment, the sample and a reference are subjected to a controlled temperature program, and the difference in heat flow between them is recorded as a function of temperature or time. This allows the determination of characteristic transition temperatures and enthalpy changes related to processes such as melting, crystallization, glass transition, or thermal decomposition[121].

For liquid electrolytes, the glass transition temperature (T_g) provides valuable insight into the molecular mobility. A lower T_g generally corresponds to higher molecular mobility and higher ionic conductivity, while a higher T_g indicates restricted ion motion and reduced conductivity[122].

In this work, DSC measurements were performed on a TA Instruments DSC 250. Samples were filled in hermetic aluminum pans in an argon-filled glovebox. DSC traces

were recorded during heating from 123 to 373 K at a rate of 10 K/min. The glass transition was defined as the midpoint of the step in the DSC curve. (Figure 3.6)

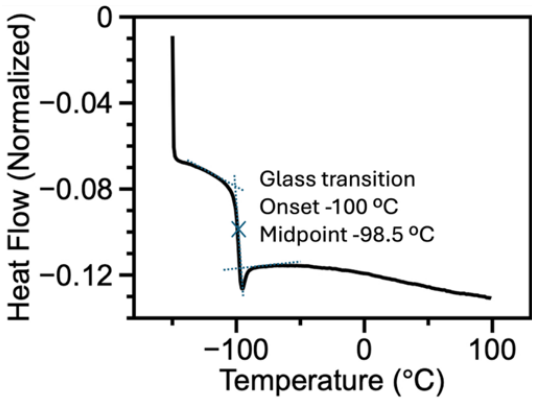

Figure 3.6. Example of DSC trace from DAIL and the obtained glass transition temperature (T_g).

3.2.3 Dielectric Spectroscopy

The temperature dependence of the ionic conductivity was determined by dielectric spectroscopy using a Novocontrol broadband dielectric spectrometer in the frequency range 10^2-10^7 Hz. The sample was placed between two stainless steel electrodes with a Teflon spacer (diameter 20 mm and thickness 3 mm) and loaded into a cryo-furnace. The cell was assembled in argon atmosphere. Data was collected in steps of 10 ºC in the temperature range –150 to 100 ºC during cooling. The temperature equilibration time was 10 minutes.

This method enables the determination of the temperature dependence of ionic conductivity, often described by the Arrhenius or Vogel-Tammann-Fulcher (VTF) behavior[123]. Based on this, the DC conductivity was extracted from the high-frequency plateau in the frequency-dependent conductivity plot. (Figure 3.7)

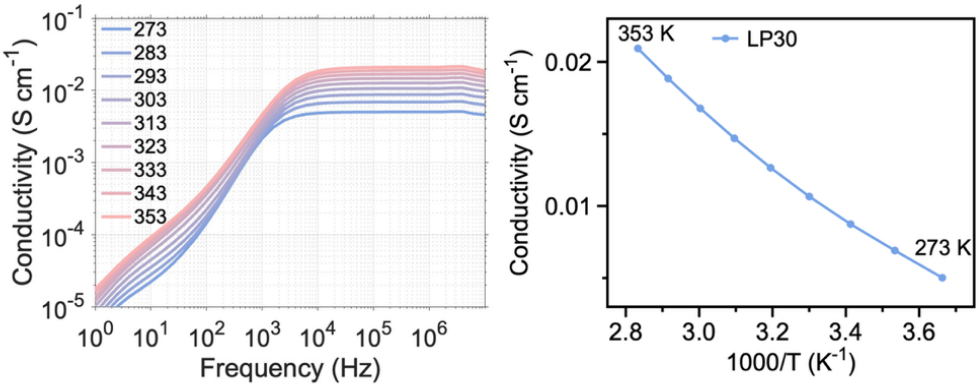

Figure 3.7. Left: real part (σ′) of the complex conductivity (σ∗(ω)=σ′(ω)+jσ′′(ω)), as a function of frequency of LP30 electrolyte obtained from dielectric spectroscopy. The bulk ionic conductivity was calculated by the average of σ′ at the high-frequency plateau. Right: DC conductivity as a function of temperature of LP30 electrolyte.

3.2.4 Viscometry and densitometry

The viscosity of the electrolytes was determined by a Lovis 2000 M/ME (Anton Paar) viscosity meter in the temperature range 10 °C - 80 °C in steps of 10 °C. Density was measured using an Anton Paar DMA 4500 M oscillation U-tube densitometer in the same temperature range. (Figure 3.8)

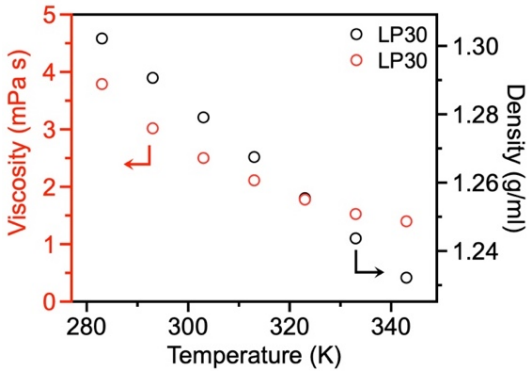

Figure 3.8. Temperature dependent viscosity and density for LP30.

3.2.5 Auger Scanning Electron Microscopy

Auger-SEM was performed with a PHI 700 Scanning Auger Nanoprobe, with a Schottky field emission electron source. For secondary electron imaging, the accelerating voltage was set to 3 kV and the beam current to 1 nA, for which no beam damage was observed. All samples were transferred to the instrument in a transfer vessel to avoid exposure to air.

3.2.6 Focused Ion Beam-Scanning Electron Microscopy

Focused Ion Beam-Scanning Electron Microscopy (FIB-SEM) used for imaging electrodes with vacuum protection with a Tescan GAIA3 FIB-SEM. Imaging was carried out at 10 keV, using an inlense secondary electron (SE)-detector.

3.2.7 X-Ray Photoelectron Spectroscopy

X-ray Photoelectron Spectroscopy (XPS) is a surface-sensitive analytical technique used to determine the elemental composition, chemical state, and electronic structure of materials[124]. It is based on the photoelectric effect, where core electrons are ejected from atoms upon irradiation with monochromatic X-rays. By measuring the kinetic energy of the emitted electrons, the binding energies of the corresponding core levels can be calculated, providing element-specific and chemical state information[125,126]. Since photoelectrons originate from only a few nanometers below the surface, XPS is particularly suitable for analyzing thin films and interfacial layers.

XPS is extensively used to investigate the composition and chemical nature of the SEI formed on electrode surfaces during cycling[126]. Here, XPS measurements were performed to analyze SEI. Prior to the experiments, the electrodes were washed with dimethyl carbonate to remove residual electrolyte from the surface and subsequently dried for 120 min under vacuum at room temperature to remove residual dimethyl carbonate solvent. The process was performed in an argon glovebox (MBraunLabstar, H_2O < 1 ppm, O_2 < 1 ppm). An argon-atmosphere-controlled transfer chamber was

employed to transfer samples from the glovebox to the XPS systems (PHI 5800, Physical Electronics). The measurements were performed under an argon atmosphere using AlK_a radiation (200W, 13 kV), at a pressure of 1.33^{-7} Pa. The spectra were calibrated to the binding energy of the C 1s peak (BE = 284.8 eV). All spectra were fitted by the deconvolution software Casa XPS (Casa Software). Gaussian-Lorentzian (30 % Gaussian) functions and a Shirley type background were employed in fitting of spectra.

3.3 Electrochemical characterization

3.3.1 Tafel plot

Data for the Tafel plot was measured in Li//Li symmetric cells by a Biologic battery test system. The voltage range was –0.2 V to 0.2 V, current density was 0.2 mA cm^{-2}. (Figure 3.9) For a Li electrode at an equilibrium potential for the Li^+/Li redox couple, an equilibrium on the electrode surface is formed by the reduction of Li^+ to Li and the oxidation of Li to Li^+, that both occur at the same rate, just as for equilibrium states in other chemical processes. The current density at equilibrium can be written as $I = I_a + I_c = 0$, where I_a and I_c are the partial anodic and cathodic current densities, respectively. The magnitude of these partial current densities at equilibrium, which is an indicator of the electron-transfer activity on the electrode surface at the equilibrium potential, has been identified as an intrinsic parameter of the kinetics on the electrode surface and is known as the exchange current density $I_0 = I_a = -I_c$ [127]. A higher I_0 means that extensive oxidation and reduction reactions occur, while a lower value indicates the opposite. In the case of Li deposition, I_0 is a crucial parameter to understand the kinetics of the electron-transfer activity on the electrode for the reduction process of Li^+ to Li[127].

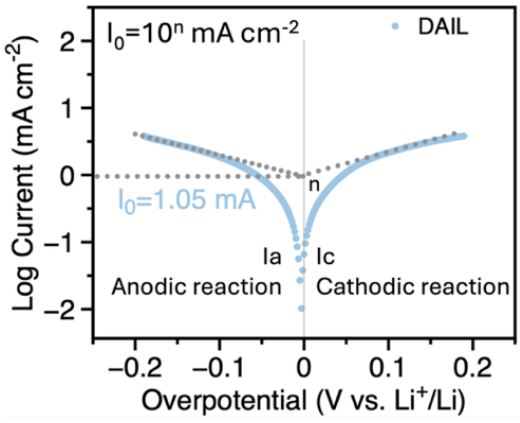

Figure 3.9. Tafel plot to calculate exchange current density for DAIL at 80 ºC.

3.3.2 Electrochemical impedance spectroscopy

Electrochemical impedance spectroscopy (EIS) is a powerful technique for characterizing the electrochemical properties and interfacial processes of battery materials. It involves applying a small-amplitude alternating voltage to an electrochemical cell over a wide frequency range and measuring the resulting current response[128]. The obtained impedance spectra reflect the frequency-dependence of, for instance, charge transfer, ion transport, and interfacial polarization processes occurring within the system.

In lithium-metal batteries, EIS is widely employed to investigate interfacial kinetics and stability at the electrode-electrolyte interface. By modeling the impedance spectra using equivalent electrical circuits, parameters such as the electrolyte resistance ($R_{electrolyte}$), charge transfer resistance (R_{ct}), SEI resistance (R_{SEI}), and double-layer capacitance (C_{dl}) can be extracted[128]. The low-frequency region of the spectrum often reveals information related to ion diffusion or mass transport within the electrolyte and SEI layer.

In this thesis, EIS experiments were performed on Li//Li symmetric cells after 50 cycles at the current density of 0.2 mA cm^{-2}. The activation energy of charge transfer and diffusion across SEI was determined by measuring EIS every 10 ºC in the temperature range of 20-80 ºC by a Biologic battery test system. (Figure 3.10a) The EIS results were fitted by EC-lab software. The simulated equivalent circuit is shown in Figure 3.10b, and composed of the internal resistance, a charge-transfer resistance parallel with a capacitance of the double layer, and a SEI resistance in parallel with a capacitance of the SEI. In LMBs, the charge transfer reaction corresponds to the desolvation process, and the resistance of SEI corresponds to the Li^+ transport through the SEI (Figures 3.10 c,d). The activation energy (E_a) for these two processes can be calculated by the Arrhenius equation: $\ln\left(\frac{T}{R_{ct/SEI}}\right) = -\frac{E_a}{RT} + lnA.$

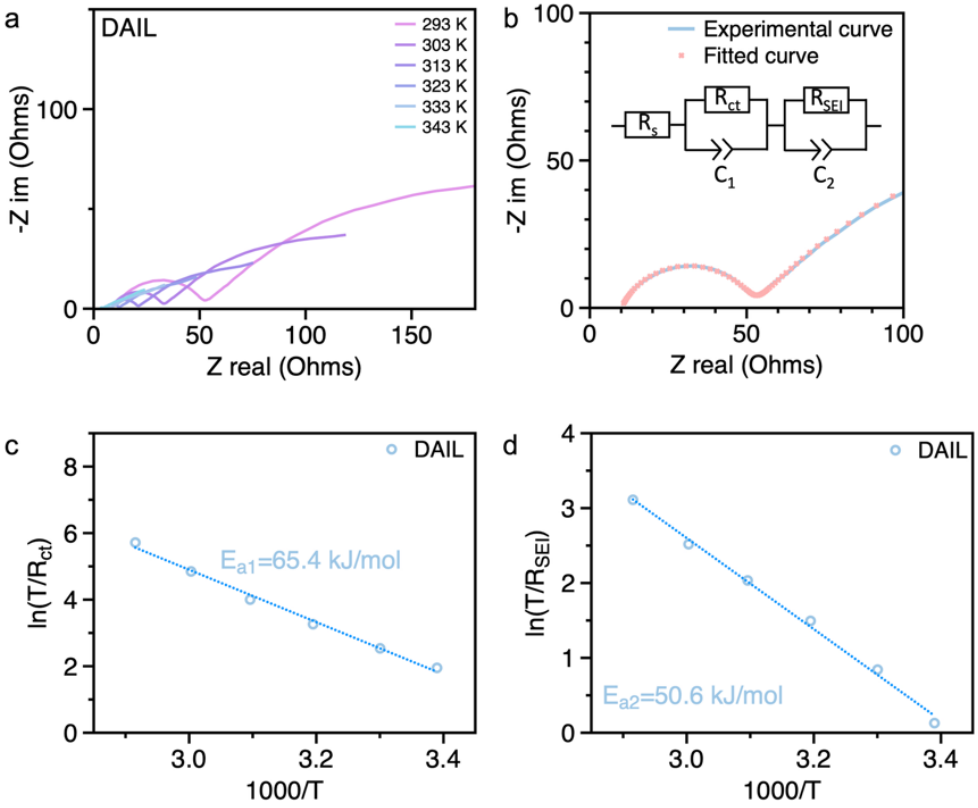

Figure 3.10. a,b) Results from EIS on DAIL of Li//Li symmetric cell; c, d) Arrhenius plots for charge transfer resistance and SEI resistance, respectively. (Activation energy for Li^+ desolvation and Li^+ diffusion through SEI are calculated from the fit with the Arrhenius equation.)

In situ EIS was performed in a Li//Cu cell in three steps[129]. The first step consists of a potential hold at 0.05 V for 5 min to form the SEI, followed by an EIS measurement,

followed by an open voltage for one hour, repeated seven times. In the second step, a constant discharge current (0.1 mA cm^{-2}) was applied for one minute to plate Li on Cu, followed by an EIS measurement, followed by a hold at open circuit for one hour, repeated eleven times. In the third step, a constant charging current of 0.1 mA cm^{-2} was applied to strip Li from Cu for one minute, followed by an EIS measurement, hold at an open circuit voltage for one hour, repeated ten times. (Figure 3.11)

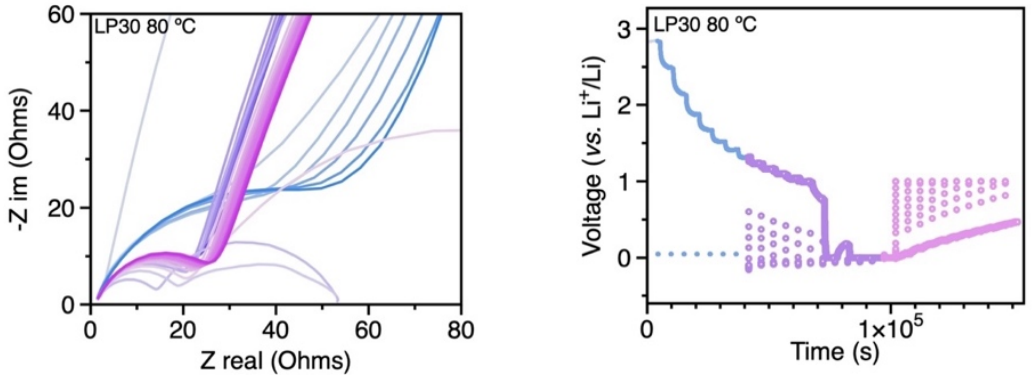

Figure 3.11. *In situ* EIS results and the corresponding voltage profile for LP30.

3.3.3 Linear sweep voltammetry

Linear Sweep Voltammetry (LSV) is an electrochemical technique used to evaluate the redox stability of electrolytes, i.e. to determine the electrochemical stability window of electrolytes. In this method, the potential of the working electrode is linearly varied with time relative to a reference electrode while the resulting current is recorded. The resulting current-potential curve provides information about at what voltage oxidation and reduction start in the electrolyte[130]. During an anodic sweep, the onset of an oxidation current indicates the upper potential limit, while during a cathodic sweep, the appearance of reduction current marks the lower potential limit.

In this thesis, LSV was performed using a Biologic battery test system. Li//stainless steel cells with different electrolytes were used for LSV. The sweep voltage range was from open circuit voltage to 5 V, at a scan speed of 1 mV s^{-1}. (Figure 3.12)

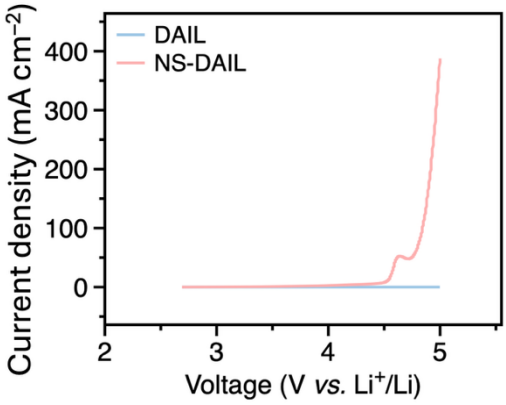

Figure 3.12. LSV results to determine the electrochemical stability window of the DAIL and NS-DAIL electrolytes.

3.3.4 Cyclic voltammetry

Cyclic voltammetry (CV) is used to study the redox behavior and interfacial reactions of electrode materials. In a CV experiment, the potential of the working electrode is linearly swept between two defined limits, and then reversed, at a controlled scan rate while the resulting current is recorded. The obtained current-potential profiles (voltammograms) provide qualitative and quantitative information about electrochemical reactions, reversibility, and kinetics of processes occurring[131]. In this work, CV was performed in Li//stainless steel cells at a scan speed of 0.1 mV s^{-1} in the voltage of 0-2.5 V with a Biologic battery test system. (Figure 3.13)

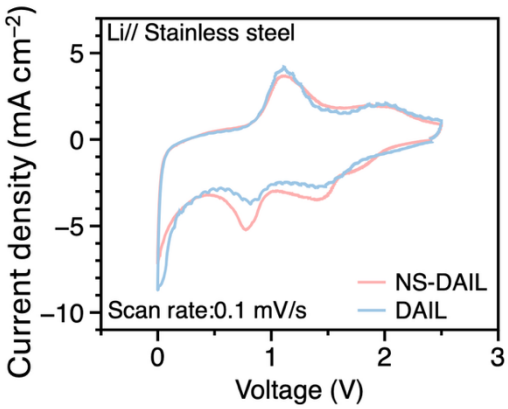

Figure 3.13. CV curves of DAIL and NS-DAIL electrolytes.

3.3.5 Galvanostatic charge and discharge

Symmetric Li//Li cells were assembled to investigate the overpotential and cycling stability of different electrolytes by a Scribner 585 battery test system. Cycling was performed by 1 h plating and 1 h stripping at the current density of 0.2 mA cm^{-2}. (Figure 3.14)

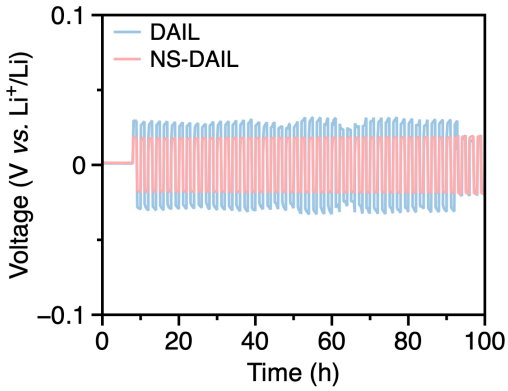

Figure 3.14. Cycling of symmetric Li//Li cells at 0.2 mA cm^{-2} with DAIL and NS-DAIL electrolytes.

Li//Cu cells were used for exploring the Coulombic efficiency of electrolytes[132]. The test procedures consist of two cycles of 15 h plating and stripping, cut-off voltage 1 V, to avoid side reactions on the Cu surface, followed by 15 h plating, and 10 cycles of 1 h stripping and 1 h plating, and finally stripping until the voltage reaches 1 V. A current density of 0.2 mA cm^{-2} was used in all experiments. The Coulombic efficiency was

calculated by the total capacity of plating and stripping, except for the initial two cycles. (Figure 3.15)

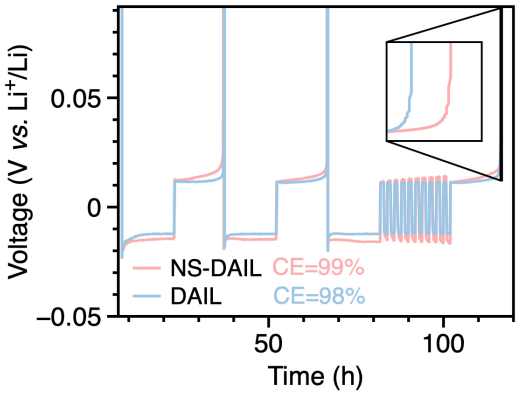

Figure 3.15. Plating and stripping test for Coulombic efficiency determination in Li//Cu cell with DAIL and NS-DAIL electrolytes.

Rate performance was performed in Li//LFP full cells at current densities of 10, 20, 50,100, 200, and 10 mA g^{-1} to study the charge/discharge abilities and stability of electrode materials at different rates, particularly at high rate.

Limited Li//LFP full cells were used to investigate the cycling performance of LMBs at close-to-practical conditions in the voltage range of 2.5-4 V. Limited Li with a thickness of 20 μm was obtained by a rolling machine.

3.3.6 Scharifker-Hills model

Chronoamperometry coupled with the Scharifer-Hills (S-H) model was employed to analyze the Li nucleation mechanism at deposition[133,134]. Li deposition was performed in Li//Li cells by stepping the working electrode potential to a fixed overpotential (–50 mV) vs. Li/Li^+ for 15 min, and the resulting current-time (I-t) transients were recorded with high time resolution. The transients were normalized by the maximum current (I_m) and corresponding time (t_m) and compared with theoretical S-H curves to distinguish between instantaneous and progressive nucleation modes (Figure 3.16).

instantaneous nucleation: $(\frac{i}{i_m})^2 = 1.9542(\frac{t}{t_m})^{-1}\{1 - \exp\left[-1.2564\left(\frac{t}{t_m}\right)\right]\}^2$ (1)

progressive nucleation: $(\frac{i}{i_m})^2 = 1.2254(\frac{t}{t_m})^{-1}\{1 - \exp\left[-2.3367\left(\frac{t}{t_m}\right)^2\right]\}^2$ (2)

where I and t are the current density and time, respectively, and I_m and t_m are the maximum values of the current transients.

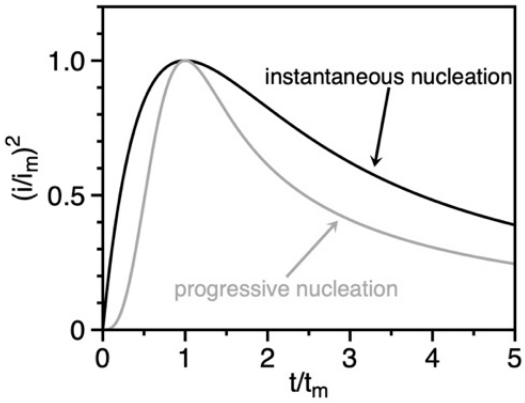

Figure 3.16. Scharifer-Hills (S-H) model of I-t curves describing instantaneous nucleation and progressive nucleation modes.

4 Results and discussion

4.1 Solvation structure

To figure out the spectral contributions of the different components, two sets of single-anion IL reference electrolytes were measured: (i) FSI-based systems (LiFSI-Pyr_{14}FSI, LiFSI-Pyr_{14}FSI-SL, and LiFSI-Pyr_{14}FSI-SL-$LiNO_3$) and (ii) TFSI-based systems (LiTFSI-Pyr_{14}TFSI, LiTFSI-Pyr_{14}TFSI-SL, and LiTFSI-Pyr_{14}TFSI-SL-$LiNO_3$), with compositions summarized in Tables 3.1 and 3.2 in 3.1.1. Deconvolution of the spectra (Figure 4.1a,b) revealed that contact ion pairs (CIP), and aggregate (AGG) of FSI and solvation separated ion pairs (SSIP) FSI appear at 733, 748, and 724 cm^{-1}, respectively, while CIP of TFSI is located at 747 cm^{-1} and the two SSIP conformers (C1 and C2) at 739 and 741 cm^{-1}[1135]. These reference assignments enabled the deconvolution of the Raman spectra from DAIL and NS-DAIL into six components (Figure 4.2a). One can note that the spectral components corresponding to TFSI are considerably narrower, which allows separation of contributions from FSI and TFSI which are at similar wavenumbers.

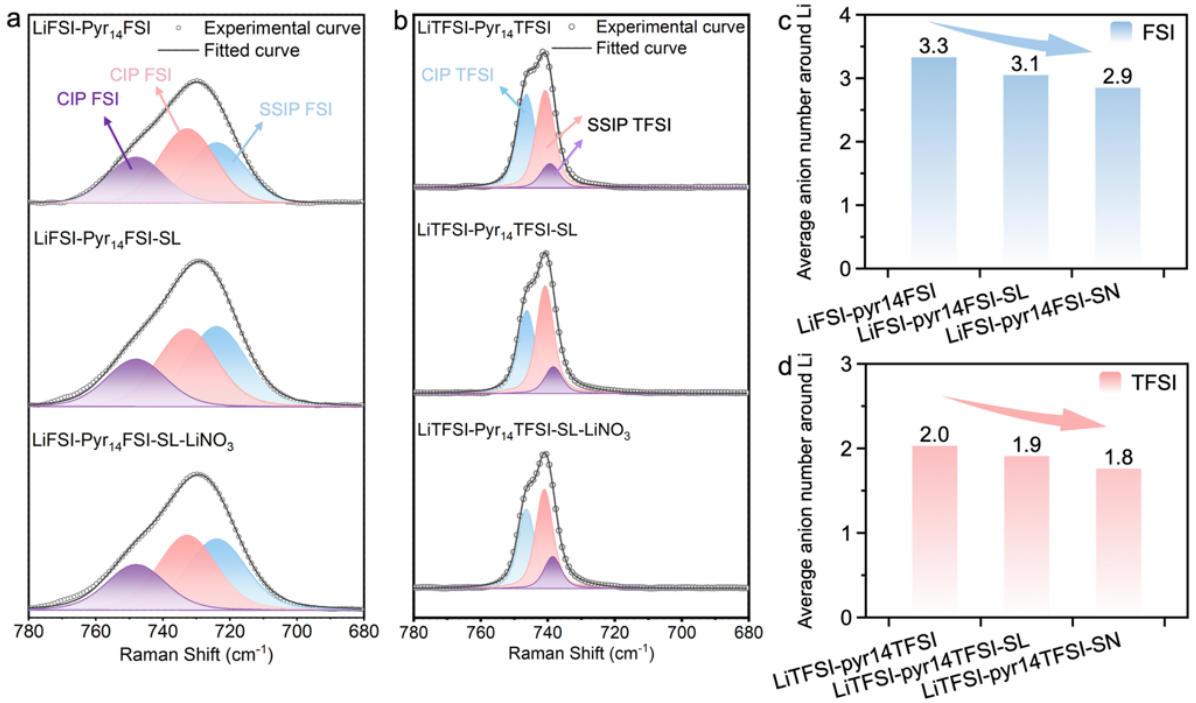

Figure 4.1. Raman spectra of reference electrolytes with one anion. a) LiFSI-Pyr_{14}FSI (top), LiFSI-Pyr_{14}FSI-SL (middle), LiFSI-Pyr_{14}FSI-SL-$LiNO_3$ (bottom); b) LiTFSI-Pyr_{14}TFSI (top), LiTFSI-Pyr_{14}TFSI-SL (middle), LiTFSI-Pyr_{14}TFSI-SL-$LiNO_3$ (bottom). Average number of anions around Li^+ in c) single FSI-based ILEs, and d) single TFSI-based ILEs.

Quantitative analysis of the average coordination numbers of TFSI and FSI coordinated to one Li^+ was carried out to further elucidate the change of coordination structure (derived from integrated, normalized peak areas; see 3.2.1 for methods)[118,119]. The results are shown in Figure 4.2 b, the average number of FSI coordinated to Li^+ decreases from 2.7 to 2.1, whereas the number of TFSI coordinated to Li^+ decreases

from 0.5 to 0.4 with the addition of SL and $LiNO_3$. The reduction of the number of anions around Li^+ shows that the addition of SL and $LiNO_3$ weakens the interaction of Li^+ to TFSI and FSI. Furthermore, the average number of anions coordinated to Li^+ of the single-anion ILEs shows a similar decrease (Figures 4.1 c and d) with the introduction of only SL and the mix of SL-$LiNO_3$, further verifying that incorporation of SL and $LiNO_3$ species with high donor numbers effectively weakens Li^+-anion coordination[118,119].

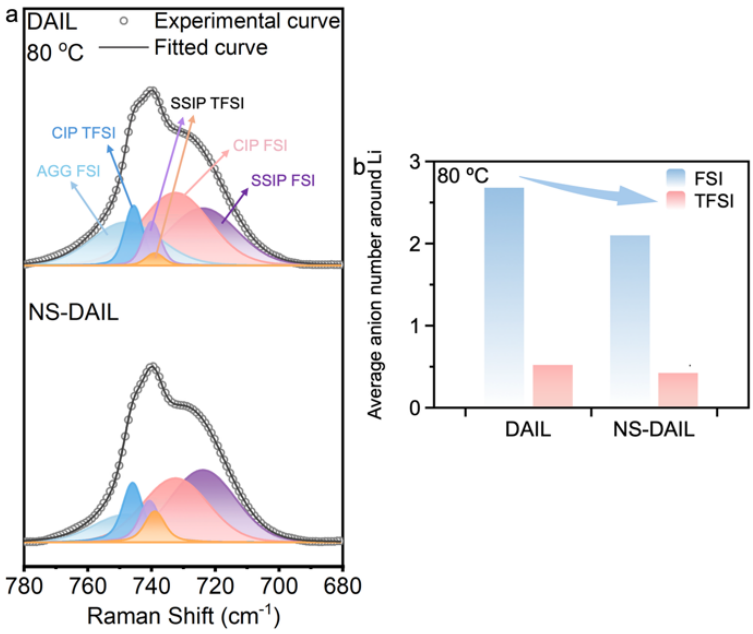

Figure 4.2. Raman spectra from DAIL and NS -DAIL at 80°C in the region of the FSI and TFSI symmetric vibrational contributions and the fit to the spectra with six bands. Bands correspond to SSIP, CIP, AGG of FSI, CIP of TFSI, and two conformers (cisoid and transoid) of free TFSI (SSIP), respectively. b) Average number of anions around Li^+.

A parallel analysis was employed to investigate the solvation structure of Li^+ of LP30 and Pyr_{14}FSI-LP30 at 80 °C. In pristine LP30 (Figure 4.3), characteristic peaks at 716 and 727 cm^{-1} arise from the ring-bending vibrations of free and coordinated EC ($Li(EC)_4$), while a feature at 740 cm^{-1} corresponds to SSIPs of PF_6^-. Upon introducing Pyr_{14}FSI, an additional band at 746 cm^{-1} emerges, indicative of CIPs of PF_6^-, accompanied by peaks at 723 and 727 cm^{-1} assigned to FSI SSIPs and CIPs. Normalized spectra (Figure 4.3) show increased intensity in the 720-735 and 745-750 cm^{-1} regions for 10 and 20 wt% Pyr_{14}FSI-LP30, evidencing the stronger involvement of FSI and PF_6^- in Li^+ solvation.

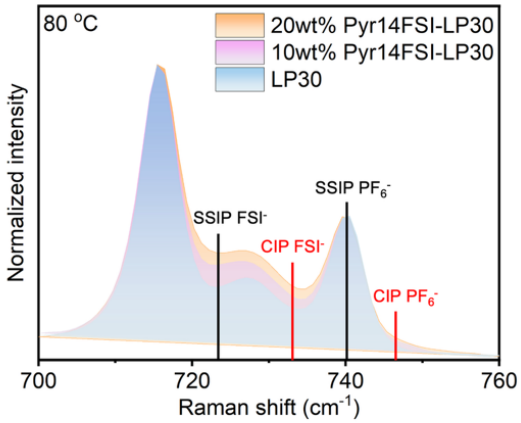

Figure 4.3. Raman spectra from LP30, 10wt%Pyr_{14}FSI-LP30, and 20wt% Pyr_{14}FSI-LP30 at 80 ºC, in the region of the FSI and PF_6^- vibrational contributions with intensity normalized to the intensity of the peak located at 717 cm^{-1}.

Peak deconvolution further reveals decreasing intensity of bands corresponding to coordinated EC and DMC, while coordinated anion bands increase with increasing Pyr_{14}FSI content (Figure 4.4a). Figure 4.4b shows ring-breathing vibration of free EC (892 cm^{-1}), coordinated EC (903 cm^{-1}), the C-O stretching vibration of free DMC (914 cm^{-1}), and coordinated DMC (930 cm^{-1}), which also confirms the reduced participation of carbonate solvents in the primary solvation shell of Li^+. These changes stem from the stronger Lewis basicity of FSI compared to carbonate solvents and the weak interaction of the bulky, charge-delocalized Pyr_{14}^+.

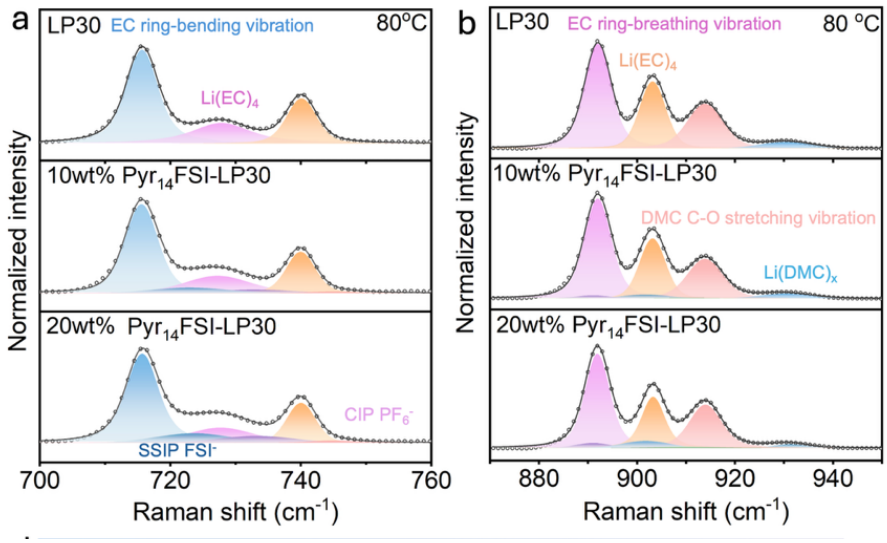

Figure 4.4. Raman spectra at 80 ºC a) in the region of the FSI and PF_6^- vibrational contributions and the fit to the spectra with six bands, and b) in the region of the EC and DMC vibrational contributions and the fit to the spectra with four main bands. LP30 (top), 10wt%Pyr_{14}FSI-LP30 (middle), 20wt%Pyr_{14}FSI-LP30 (bottom).

Quantitative analysis of coordination numbers (Figure 4.5) shows a clear decrease in solvent coordination and an increase in anion coordination, marking a shift from solvent-dominated to anion-solvent mixed solvation environments with the introduction of ionic liquid.

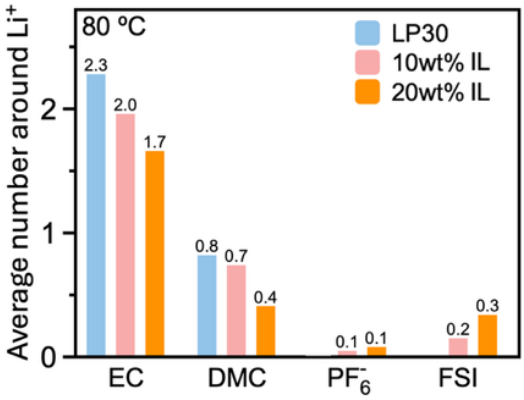

Figure 4.5. Average number of solvent molecules (EC and DMC) and anions (PF_6^-, and FSI-anion) around Li^+ at 80 ºC, calculated from the integrated intensities of Raman bands.

Raman spectroscopy provides clear evidence that both electrolyte design strategies explored in this thesis successfully reconfigure the Li^+ solvation environment in fundamentally different yet functionally convergent ways. In the ionic liquid system, the addition of sulfolane and $LiNO_3$ decreases the average number of coordinated FSI and TFSI, indicating that high donor number additives partially displace anions from the primary solvation shell. In the carbonate system, introducing $Pyr_{14}FSI$ shifts the solvation structure in the opposite direction by suppressing solvent coordination and enriching the solvation shell with FSI and PF_6^-.

Despite originating from two opposite solvation regimes of anion-coordinated (DAIL) and solvent-dominated (LP30), both approaches ultimately converge toward an anion-solvent mixed solvation structure. This convergence directly supports improved interfacial desolvation behavior, promotes inorganic-rich SEI formation, and underscores that targeted solvation-shell engineering is a versatile and effective method for stabilizing Li metal anodes at elevated temperatures.

4.2 Li^+ transfer kinetics

The transfer kinetics of Li^+ in DAIL and NS-DAIL for high-temperature LMBs were investigated to elucidate the correlation between interfacial charge transfer and Li^+-anion coordination. The exchange current density (I_0) determined from Tafel plots (Figure 4.6) is a key descriptor of interfacial kinetics, reflecting the intrinsic rate of Li^+ transfer across the electrode-electrolyte interface under equilibrium conditions[127]. NS-DAIL exhibits an I_0 of 2.5 mA cm^{-2}, which is higher than that of DAIL (1.1 mA cm^{-2}), highlighting significantly accelerated interfacial charge-transfer reactions[127]. This enhancement implies more efficient Li^+ transfer, reduced polarization, improved rate capability, and higher reversibility during cycling.

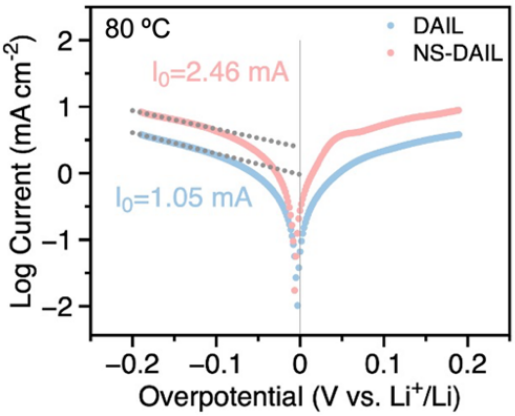

Figure 4.6. Tafel plots of DAIL and NS-DAIL from Li//Li symmetric cells to determine exchange current densities at 80 ºC.

To further probe the kinetic barriers, EIS as a function of temperature was conducted (Figure 4.7a). To extract information on the activation energy for charge transfer (E_{a1}) and diffusion across the SEI (E_{a2}), the spectra were fitted using the equivalent circuit shown in Figure 4.7b, where R_s denotes bulk resistance, R_{ct} corresponds to charge-transfer resistance associated with Li^+ desolvation, and R_{SEI} reflects SEI diffusion resistance. The activation energies (E_a) were extracted using the Arrhenius relationship:

$$\ln\left(\frac{T}{R_{EIS}}\right) = -\frac{E_a}{RT} + lnA,$$

where R_{EIS}, A, R, and T represent resistance, pre-exponential factor, gas constant, and absolute temperature, respectively[92]. As displayed in Figure 4.7c, the desolvation barrier (E_{a1}) of NS-DAIL is 41 kJ mol^{-1}, notably lower than what is found for DAIL (65 kJ mol^{-1}), confirming that weakened Li^+-FSI/TFSI coordination facilitates desolvation. Meanwhile, the interfacial diffusion barrier (E_{a2}, Figure 4.7d) is just slightly reduced in NS-DAIL (50 kJ mol^{-1}) compared with DAIL (51 kJ mol^{-1}), indicating marginally faster Li^+ migration through the SEI. Collectively, these results (Figure 4.8) demonstrate that the introduction of SL and $LiNO_3$ reduces Li^+-anion coordination strength, thereby lowering desolvation and transport barriers, which results in significantly better transfer kinetics and is essential for stable high-temperature LMBs operation.

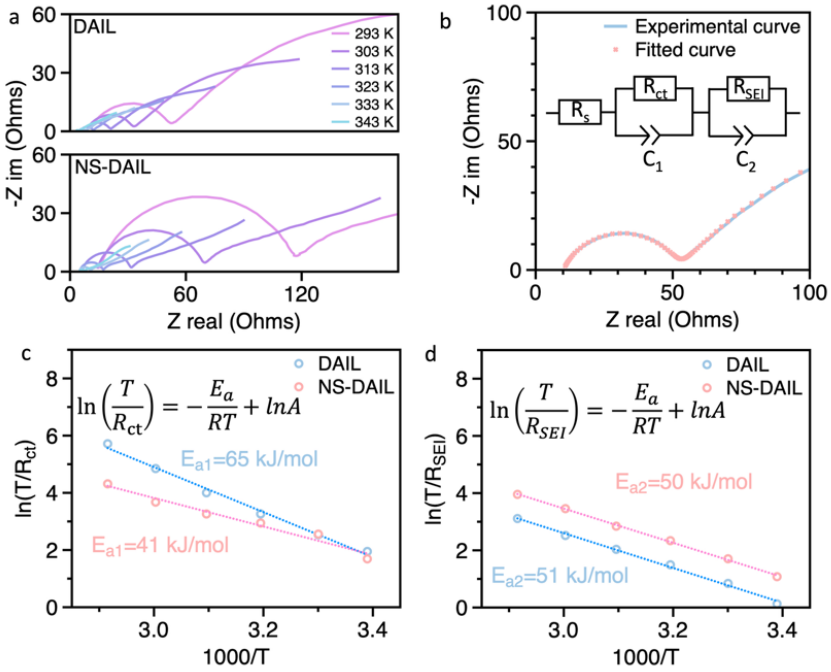

Figure 4.7. a) EIS spectra at different temperatures from Li//Li symmetric cells for DAIL and NS-DAIL. b) Example of fitted EIS of DAIL at 293 K and the fitted equivalent circuit; c) Activation energy for desolvation (E_{a1}) determined from fitted charge transfer resistances to EIS data. d) Activation energy for Li^+ diffusion through SEI (E_{a2}) from fitted SEI resistances to EIS data.

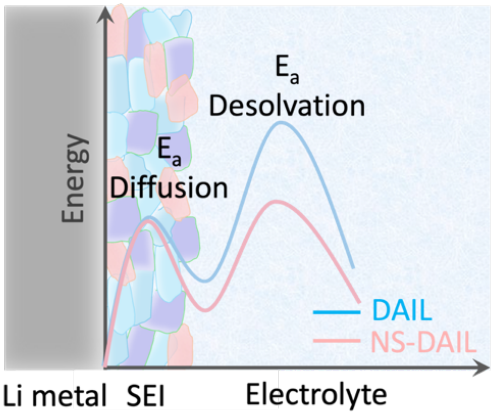

Figure 4.8. Schematic diagram of the energy barrier of Li^+ desolvation and diffusion through SEI.

For LP30 electrolyte, the exchange current density rises from 0.6 to 10.0 mA after adding 10wt% $Pyr_{14}FSI$ at 80 ºC, reflecting that the introduction of anions in the solvation shell accelerates charge transfer reactions. (Figure 4.9)

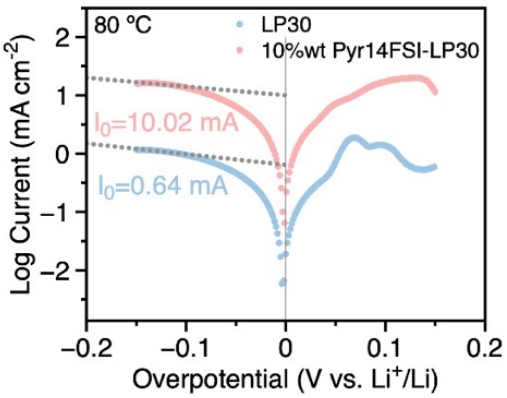

Figure 4.9. Tafel plots of LP30 and 10wt% $Pyr_{14}FSI$-LP30 from Li//Li symmetric cells to determine exchange current densities at 80 ºC.

The kinetic analysis clearly demonstrates that tailoring the Li^+ coordination environment is an effective strategy for accelerating interfacial charge transfer at metal anodes. Despite arising from different solvation mechanisms, both electrolyte strategies converge on the same outcome of accelerated Li^+ transfer.

4.3 Electric double layer structure

To gain deeper insight into the interfacial regulation by adding $Pyr_{14}FSI$ into LP30, we examined the EDL structure and ion distribution at the Li surface. These analyses clarify how the bulky, weakly coordinating Pyr_{14}^+ and flexible FSI modulate interfacial capacitance, SEI formation, and Li deposition dynamics. EIS in symmetric Li//Li cells at both 80 ºC and room temperature reveals that with 10wt% $Pyr_{14}FSI$-LP30, markedly smaller semicircles are found compared to EIS spectra from LP30 (Figure 4.10a,b). Equivalent circuit fitting shows substantial reductions in both R_{SEI} and R_{ct} (Figure 4.10c-f). The smaller mid-frequency arc indicates a lower energy barrier across the SEI, while the smaller low-frequency semicircle corresponds to faster interfacial charge transfer[72]. Notably, double-layer capacitance (C_{dl}) increases with $Pyr_{14}FSI$ concentration, suggesting a thinner, more compact EDL, which might be formed by Pyr_{14}^+ adsorption at the surface.

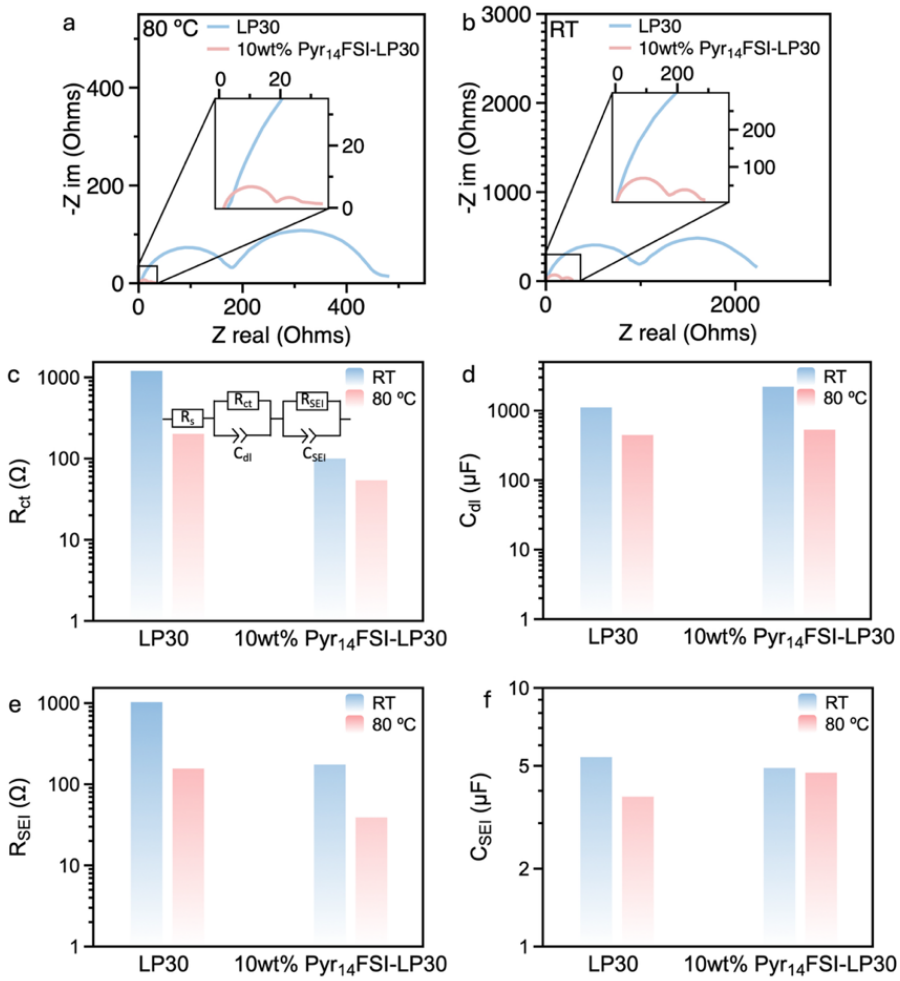

Figure 4.10. EIS spectra from Li//Li cells with LP30 and 10wt%Pyr_{14}FSI-LP30 as electrolytes at a) 80 ºC, b) room temperature. Equivalent-circuit fitting results of c) charge-transfer resistance (R_{ct}) (equivalent circuit inserted), d) double layer capacitance (C_{dl}), e) SEI diffusion resistance (R_{SEI}), f) capacitance of SEI (C_{SEI}).

4.4 SEI properties

XPS was used to analyze the composition of the SEI. In the Li 1s spectra (Figure 4.11), for both electrolytes LiF and Li_2O are found at the surface; after sputtering, a metallic Li signal appeared as the top layers were removed. Notably, electrodes cycled in NS-DAIL displayed increasing LiF intensity with longer sputtering, indicating that FSI/TFSI decomposition products are found deeper into the SEI. In the C 1s region, C-N, C-S, and C-C/C-H species dominated before sputtering, while a CF_2 peak (≈290 eV) emerged after 10 min of sputtering, which is associated with TFSI reduction[136]. The CF_2 signal was much stronger for NS-DAIL, confirming greater anion-derived SEI. In the N 1s spectra, an organic N peak from Pyr_{14}^+ (≈402.8 eV) was detected only on the electrode cycled in DAIL, showing that organic cations are incorporated into its SEI, whereas NS-DAIL forms an SEI free of cation-derived nitrogen. Quantitative analysis of C 1s components reveals a bilayer SEI structure for both electrolytes, with an organic-rich outer region and an inorganic-dominated inner layer. While the outer-layer compositions are comparable, the inner SEI formed in NS-DAIL contains fewer organic species and

significantly more inorganic species (CF_2, C-N, C-S, CO_3), indicating stronger involvement of anions and reduced incorporation of Pyr_{14}^+ compared with DAIL.

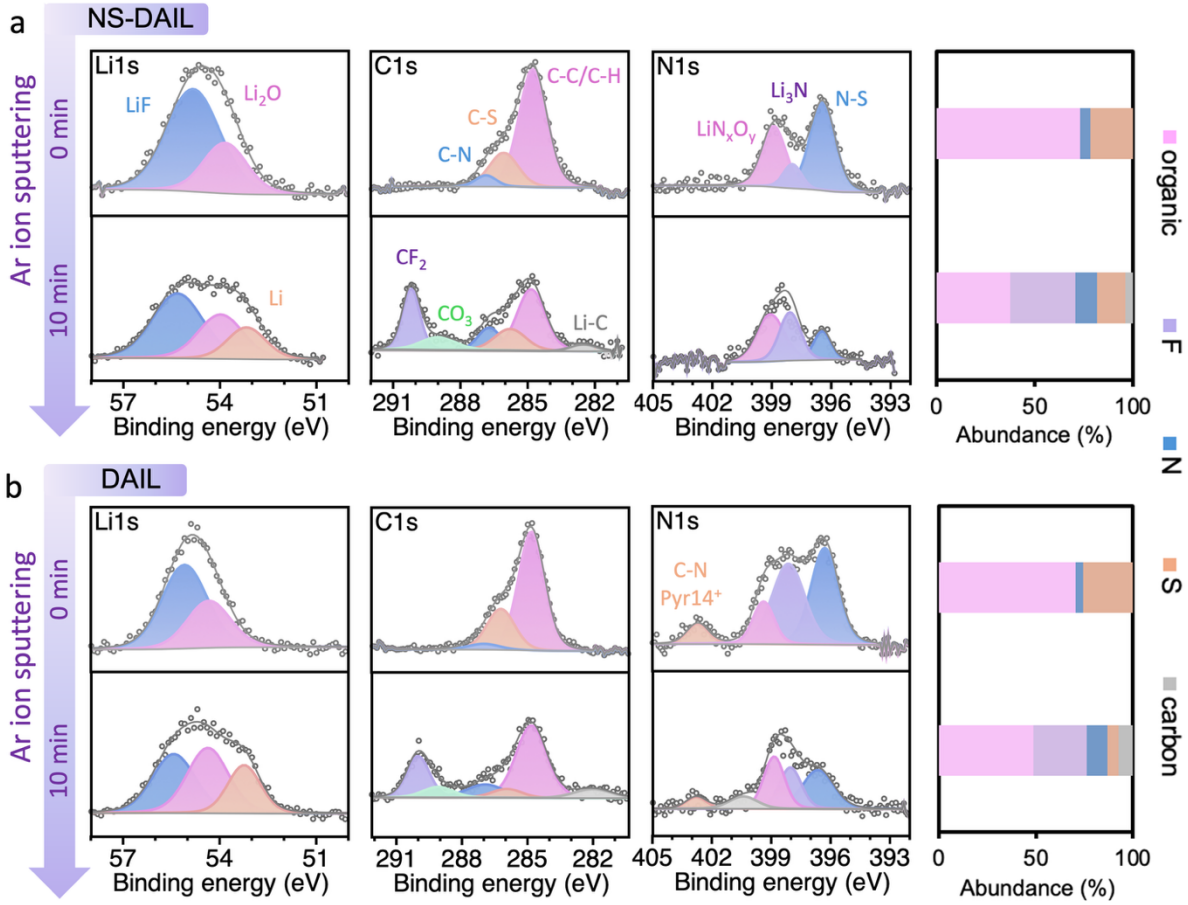

Figure 4.11. XPS spectra from Li anodes retrieved from Li//Cu cells, with 0 and 10 min Ar ion sputtering, cycled in a) NS-DAIL and b) DAIL electrolytes. Fitted results show which species contribute to the spectra.

XPS of cycled Li surfaces also further validated the solvation-structure-driven interfacial reorganization by introducing 10wt% $Pyr_{14}FSI$ into LP30 (Figure 4.12). Li anodes harvested from Li//Cu cells after 20 cycles were rinsed with DMC and vacuum-dried in an Ar-filled glovebox. In the F 1s spectra, 10 wt% $Pyr_{14}FSI$-LP30 showed stronger P-F signals than LP30, along with a distinct $-CF_2-CH_2-$ feature, confirming a PF_6^-/FSI-dominated SEI. O 1s spectra revealed a more intense $R-OCO_2Li/Li_2CO_3$ peak for LP30, indicating extensive solvent decomposition in carbonate-based electrolytes. Similarly, the P 2p doublet from PF_6^- decomposition was more pronounced in 10wt% $Pyr_{14}FSI$-LP30, underscoring greater anion participation. Overall, Li cycled in 10wt% $Pyr_{14}FSI$-LP30 developed an SEI enriched in inorganic, PF_6^-/FSI-derived species, whereas LP30 yielded an organic- and carbonate-rich interphase. The inorganic-rich SEI is mechanically robust and ionically conductive, promoting uniform Li^+ flux across the electrode.

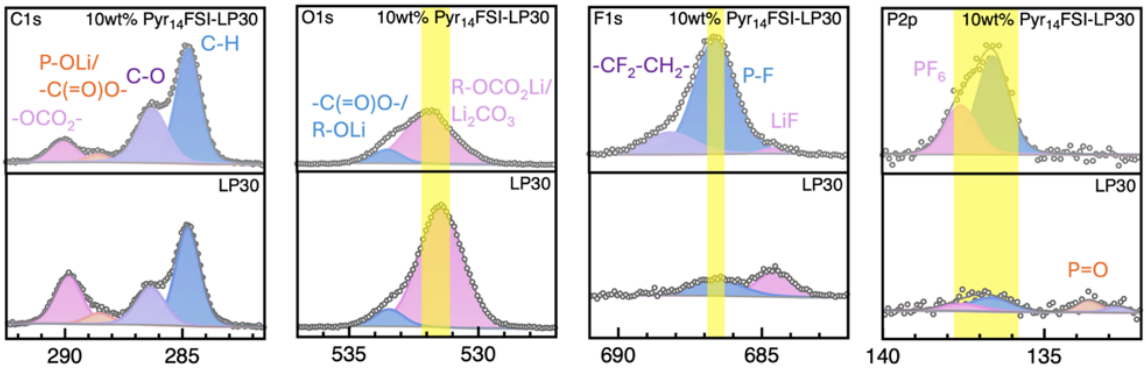

Figure 4.12. XPS spectra from Li anodes retrieved from Li//Cu cells cycled in LP30 and 10wt%Pyr_{14}FSI-LP30 electrolytes. Fitted results show which species contribute to the spectra.

XPS analysis reveals clear differences in SEI chemistry between the two electrolyte strategies, despite both ultimately promoting more inorganic and more stable interphases. For NS-DAIL, the XPS results show that anion-derived fragments (LiF, CF_2 species) dominate, while Pyr_{14}^+-derived nitrogen is absent, indicating that weakened Li^+-FSI/TFSI coordination leads to more complete Li^+ desolvation and more anion reduction within the SEI. For Pyr_{14}FSI-LP30, XPS indicates a shift from solvent-derived carbonates in LP30 to an anion-rich SEI, reflecting reduced solvent participation and enhanced PF_6^-/FSI decomposition at the Li surface. Despite their different design principles, both NS-DAIL and Pyr_{14}FSI-LP30 form SEIs that are more inorganic, chemically uniform, and ionic conductive than those produced by their respective baseline electrolytes (DAIL and LP30). The mechanisms of these two electrolyte engineering strategies are different. NS-DAIL enhances inorganic SEI formation by weakening Li^+-anion coordination, enabling highly desolvated Li^+ to reduce anions directly, whereas Pyr_{14}FSI-LP30 achieves similar SEI chemistry by reorganizing the EDL, suppressing solvent access, and promoting anion-dominated reduction at the interface.

4.5 Li plating/stripping mechanism

SEM was used to probe Li plating morphologies in DAIL and NS-DAIL. When 3 mAh Li was deposited on Cu at 0.2 mA cm^{-2}, the DAIL sample (Figure 4.13a,b) exhibited an inhomogeneous surface coverage and multiple pits. In contrast, the NS-DAIL sample (Figure 4.13d, e) showed a dense, uniform Li layer with negligible pits. Morphologies after 50 cycles in Li//LFP full cells at 100 mA g^{-1} further revealed clear differences: the DAIL anode (Figure 4.13c) displayed cracks, wrinkles, and large Li particles, evidencing preferential stripping/replating of Li^+ at certain points on the surface. Conversely, the NS-DAIL sample (Figure 4.13f) maintained a smooth, compact surface with only minor particles, reflecting reversible and homogeneous stripping/plating without interfacial hotspots. These morphological results align with the analysis of solvation structure, charge transfer kinetics, and SEI composition, confirming that tuning Li^+-anion coordination in IL electrolytes effectively optimizes plating/stripping behavior, suppresses dendrites, and enhances electrochemical stability.

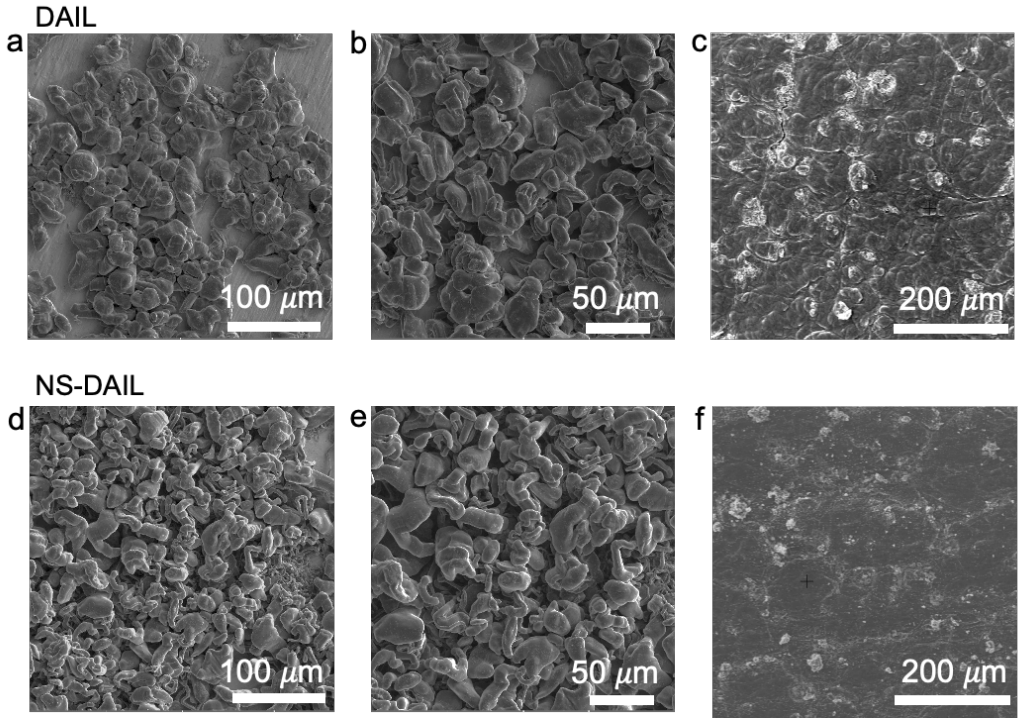

Figure 4.13. SEM images of 3 mAh Li plated on Cu at 0.2 mA cm^{-2} at 80°C in a,b) DAIL, and d,e) NS-DAIL electrolytes. SEM images of Li-metal anode surface after 50 cycles in Li//LFP full cells at 100 mA g^{-1} current density with c) DAIL and f) NS-DAIL electrolytes.

SEM was also used to investigate Li plating morphologies in LP30 and 10 wt% $Pyr_{14}FSI$-LP30 at 80 ºC (Figure 4.14). At 1.2 mA cm^{-2} with a deposition capacity of 0.12 mAh cm^{-2} at 80 °C, Li plated from LP30 showed protrusive deposition, and high-magnification images revealed volcano-like stacks with tip-growth features, characteristic of dendritic morphology. In contrast, Li plated from 10 wt% $Pyr_{14}FSI$-LP30 formed a dense, smooth surface free of dendrites, highlighting the role of interfacial reconstruction in uniformizing deposition by introducing $Pyr_{14}FSI$ into LP30.

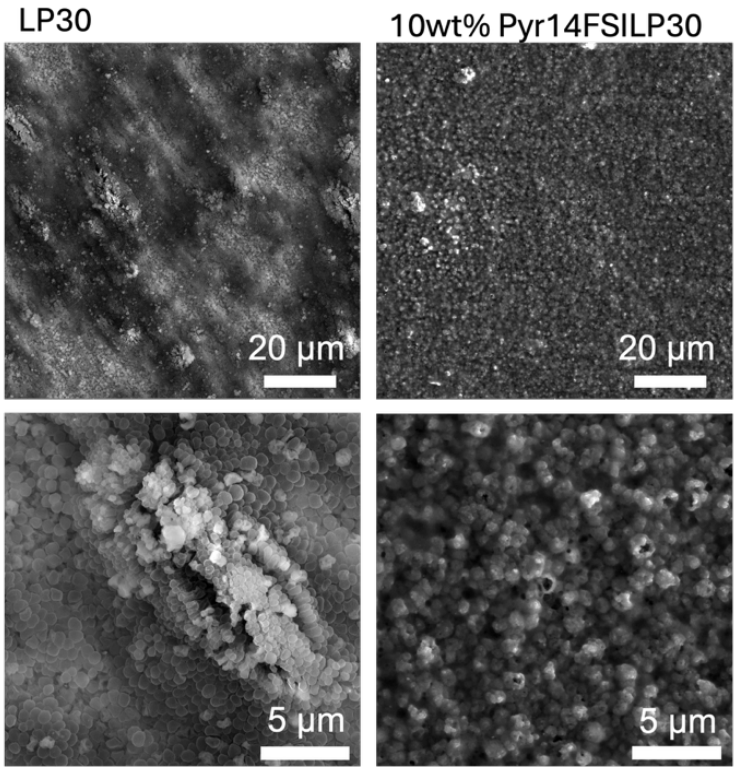

Figure 4.14. SEM images of plated Li (0.12 mAh cm^{-2} at a current density of 1.2 mA cm^{-2}) from cells cycled with LP30 (left) and 10wt%Pyr_{14}FSI-LP30 (right) at 80 ºC.

Across both electrolyte systems, SEM shows that modifying Li^+ solvation and interfacial chemistry consistently transforms Li growth from rough, dendritic to compact, and uniform. But the mechanisms are different in these two electrolyte systems. In the IL-based system, DAIL produces pitted, uneven Li due to sluggish Li^+ transport and heterogeneous interfacial ion distribution, whereas NS-DAIL yields dense and smooth deposits because weakened Li^+-anion coordination accelerates desolvation, enhances Li^+ flux, and forms an inorganic, ion-conductive SEI. In the carbonate system, LP30 generates protrusions and volcano-like dendritic structures at 80 °C, while 10 wt% Pyr_{14}FSI-LP30 produces a flat, dendrite-free morphology owing to anion-rich solvation and EDL reconstruction. Thus, although the strategies differ by coordination weakened (NS-DAIL) vs interfacial/EDL engineering (Pyr_{14}FSI-LP30), both lead to more homogeneous and dendrite-free Li plating.

4.6 Electrochemical fingerprint of the Sand's time

To clarify how the electrode-electrolyte interface evolves, we performed in-situ EIS in Li//Cu cells during SEI formation and a subsequent plating/stripping cycle (Figure 4.15). Before cycling, both electrolytes exhibit only a diffusion-controlled response in the spectra (light blue). After SEI formation, a clear semicircle appears, substantially larger in LP30 than in Pyr_{14}FSI-LP30, showing that LP30 generates a thicker or more resistive interphase (blue curves). During Li plating, the semicircle for Pyr_{14}FSI-LP30 steadily contracts, signifying enhanced charge-transfer kinetics as deposition progresses, while the low-frequency tail indicates that bulk ion transport remains sufficient to prevent strong concentration gradients (purple). In contrast, after plating in LP30, the Warburg feature is replaced by a second large semicircle, signaling transport limitation[137] and

interfacial constriction, which is an electrochemical hallmark of high-surface-area Li growth[129,138]. During stripping (magenta curves), both systems return to a single semicircle with a low-frequency tail, though the increase in resistance is modest for Pyr_{14}FSI-LP30, consistent with a thinner, more ion-conductive SEI.

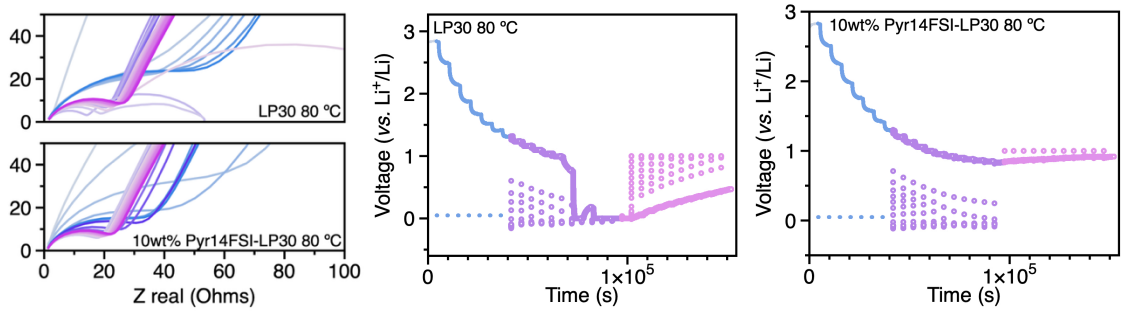

Figure 4.15. In-situ EIS spectra from Li//Cu cells with LP30 and 10wt%Pyr_{14}FSI-LP30 electrolytes at 80 ºC, and the recording voltage as a function of time during in-situ EIS of Li//Cu cells with LP30 and 10wt%Pyr_{14}FSI-LP30 electrolytes at 80 ºC. Dots with different colors represent the voltage response at different conditions. Blue: potential hold at 0.05 V for 5 min, followed by an EIS measurement, and hold at open circuit voltage for one hour, repeated 7 times. Purple: a constant current of 0.1 mA cm^{-2} was applied for 1 min to plate Li on Cu, followed by an EIS measurement and a hold at open circuit voltage for one hour, repeated 11 times. Magenta: a constant current of 0.1 mA cm^{-2} was applied for 1 min to strip Li from Cu, followed by an EIS and a hold at open circuit voltage for one hour, repeated this 10 times.

The Scharifker-Hills (S-H) model differentiates between instantaneous and progressive nucleation, which was used to study the nucleation mechanism and the reaching of the Sand's time[133,134]. Normalized current-time (I-t) transients for both electrolytes were compared with theoretical S-H curves (instantaneous: black; progressive: grey; equations 1-2 in 3.3.6, Figure 4.16). At the early stage of nucleation, the I-t curves for both LP30 and Pyr_{14}FSI-LP30 agree with the model for progressive nucleation under diffusion control, where new nuclei continue to appear and the dominant limitation is the rate at which Li^+ migrates from the bulk to each growing site. After the peak current ($t/t_m > 1$), the transient for LP30 shifts towards a behavior characteristic of instantaneous nucleation and then exhibits a sharp current decline near $t/t_m \approx 2$, signaling interfacial Li^+ depletion. In contrast, Pyr_{14}FSI-LP30 maintains a progressive-nucleation profile without a sudden current collapse, indicating that growth is not limited by Li^+ transport. These distinct nucleation pathways correlate with the SEM observations: LP30 produces protrusive deposits due to local ion depletion, promoting uneven plating and dendrite initiation. Conversely, Pyr_{14}FSI-LP30 sustains a uniform Li^+ concentration at the surface, enabling dense and dendrite-free deposition.

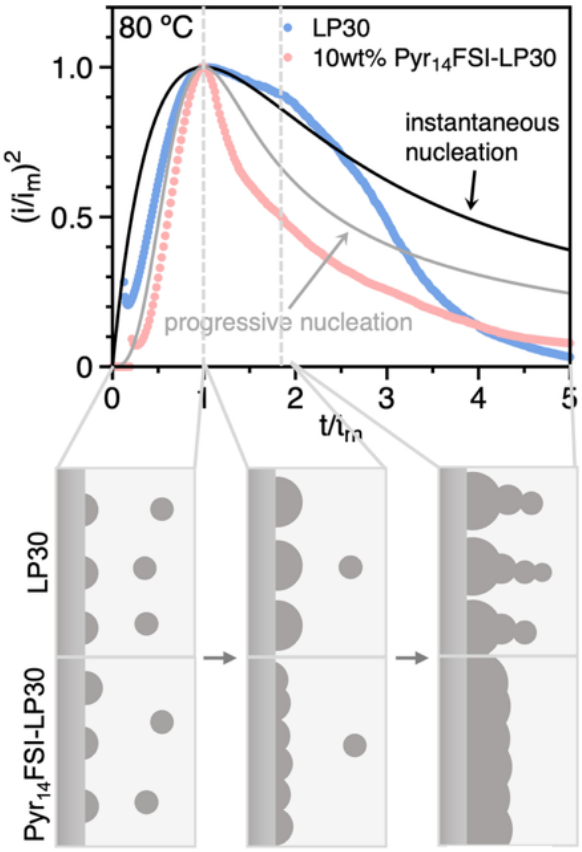

Figure 4.16. Normalized current-time (I-t) curves of LP30 and 10wt% Pyr_{14}FSI-LP30 in Li//Li cells when applying a –50 mV potential at 80 ºC.

The nucleation and growth mechanisms are schematically illustrated in Figure 4.17. In LP30, Li^+ depletion beyond Sand's time drives tip-focused growth and dendrite formation, whereas Pyr_{14}FSI-LP30 maintains interfacial ion concentration, sustaining uniform flux and enabling smooth, dendrite-free Li deposition.

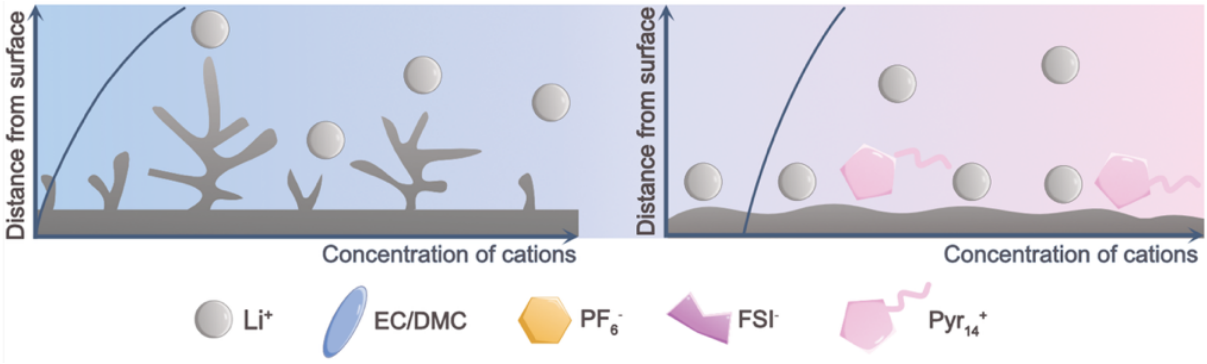

Figure 4.17. Schematic illustration of Li nucleation and growth in the presence of LP30 (left) and Pyr_{14}FSI-LP30 (right).

4.7 Electrochemical performance

The electrochemical behavior at 80 °C was evaluated to assess the practical impact of modifying the Li^+ coordination environment. LSV measured in Li//SS cells (Figure 4.18a) shows that DAIL retains oxidative stability above 5 V, whereas NS-DAIL begins to oxidize near 4.5 V, consistent with its higher fraction of weakly coordinated anions. In Li//Li symmetric cells (Figure 4.18b), the overpotential drops notably upon adding

SL and $LiNO_3$, reflecting enhanced Li^+ transport enabled by weaker Li^+-anion coordination. SEI formation was examined by CV (Figure 4.18c), where NS-DAIL exhibits an additional reduction peak around 1.8 V, indicative of easier decomposition of NO_3^-, FSI, and TFSI due to facilitated desolvation[33,139,140].

The coulombic efficiency was investigated in Li//Cu cells (Figure 4.18d), using a protocol with two initial high-capacity (3 mAh at current density of 0.2 mA cm^{-2}) plating and stripping cycles to avoid the effect of the surface side reactions on the Cu substrate. In NS-DAIL, a CE of 99% was obtained, confirming more efficient and reversible Li plating/stripping. The improved kinetics are further verified by superior rate capability in Li//LFP cells at 80 °C (Figure 4.18e), particularly at high currents. NS-DAIL achieved a specific capacity of 124 mAh g^{-1} at 200 mA g^{-1}, outperforming DAIL (102 mAh g^{-1} under identical conditions). This demonstrates the superior high-current performance of NS-DAIL, enabled by accelerated ion transfer kinetics.

For a LMB in a real application, a limited Li reservoir should be used to maximize the energy density. Thus, the practical applicability was examined using limited-Li//LFP full cells (20 µm Li thickness, Figure 4.18f). With DAIL, capacity fades after ~50 cycles and CE declines to 84% by cycle 100. In contrast, NS-DAIL supports an initial capacity of 142 mAh g^{-1}, maintains an average CE of ~99.99 %, and retains over 98% of its capacity after 180 cycles. Overall, the performance gains achieved with NS-DAIL arise from more reversible Li deposition and accelerated Li^+ transport, both directly linked to the intentionally weakened Li^+-anion coordination in the modified ionic-liquid electrolyte.

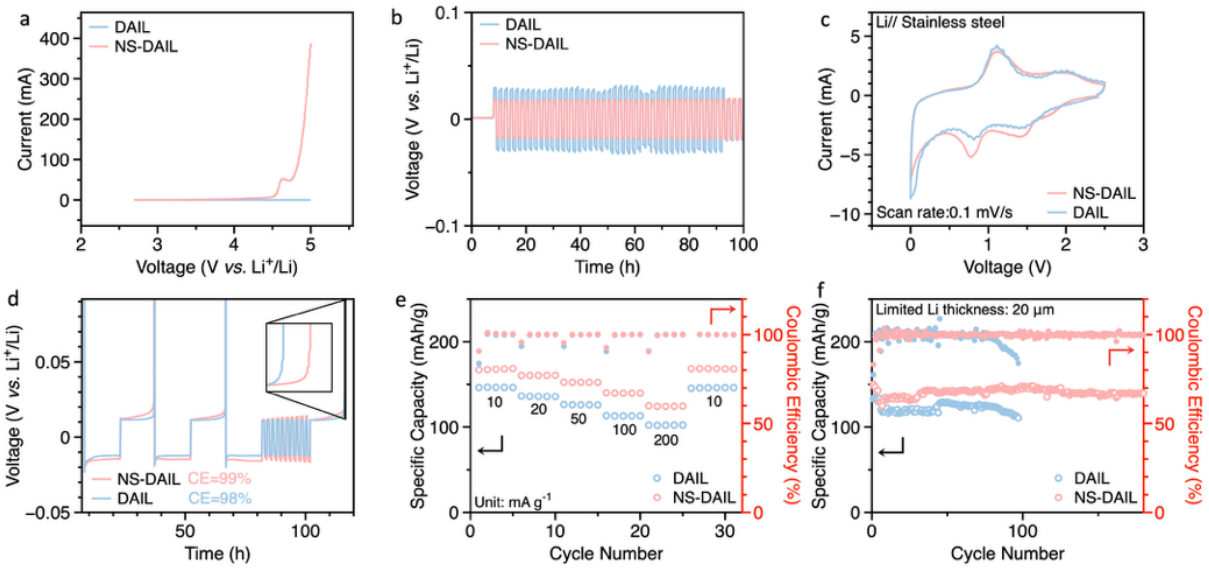

Figure 4.18. Electrochemical performance of DAIL and NS-DAIL at 80 ºC. a) Linear sweep voltammetry in Li//SS cells at 1 mV s^{-1}. b) Cycling performance of symmetric Li//Li cells at 0.5 mA cm^{-2}. c) Cyclic voltammetry in the voltage range of 0-2.5 V on Li//stainless steel cells with a scan rate of 0.1 mV s^{-1}. d) Coulombic efficiency test in Li//Cu half cells. e) Rate performance in Li//LFP full cells. f) Long term cycling performance in limited Li//LFP full cells with 20 µm Li anode thickness.

Electrochemical studies demonstrate that the addition of $Pyr_{14}FSI$ into LP30 fundamentally alters interfacial chemistry and stabilizes Li cycling (Figure 19). While the oxidative stability slightly decreases (~4 V vs. >5 V for LP30), the modified electrolyte delivers markedly enhanced kinetics: in Li//Li cells, the overpotential drops from 21 to 4 mV, highlighting that anion-enriched solvation lowers desolvation barriers while the resulting inorganic-rich SEI accelerates charge transfer. In Li//Cu cells, CE improved from 93% (LP30) to 98% ($Pyr_{14}FSI$-LP30), consistent with compact Li deposition and reduced dead-Li accumulation (Figure 4.19d). The long-term cycling behavior at high rate (2C = 350 mA g^{-1}) was evaluated in LTO//Li full cells (Figure 4.19e). The electrolyte containing $Pyr_{14}FSI$-LP30 preserved 86% of its initial capacity after 50 cycles, while the LP30 counterpart began to degrade noticeably after roughly 40 cycles. To reflect practical high-energy configurations, LTO//limited-Li (20 μm) full cells were also examined (Figure 4.19f). With $Pyr_{14}FSI$-LP30, the cell delivered an outstanding ~99.9% Coulombic efficiency and maintained 93% capacity retention after 50 cycles, whereas the LP30 cell experienced rapid failure within 30 cycles. These improvements originate from a synergistic mechanism: stronger Li^+-FSI coordination reduces desolvation resistance, IL-derived inorganic SEI enhances surface energy and ion transport; delay Li^+ depletion. Collectively, these effects suppress dendritic growth, enable compact Li plating, and deliver high-efficiency, stable cycling under both ambient and elevated temperatures.

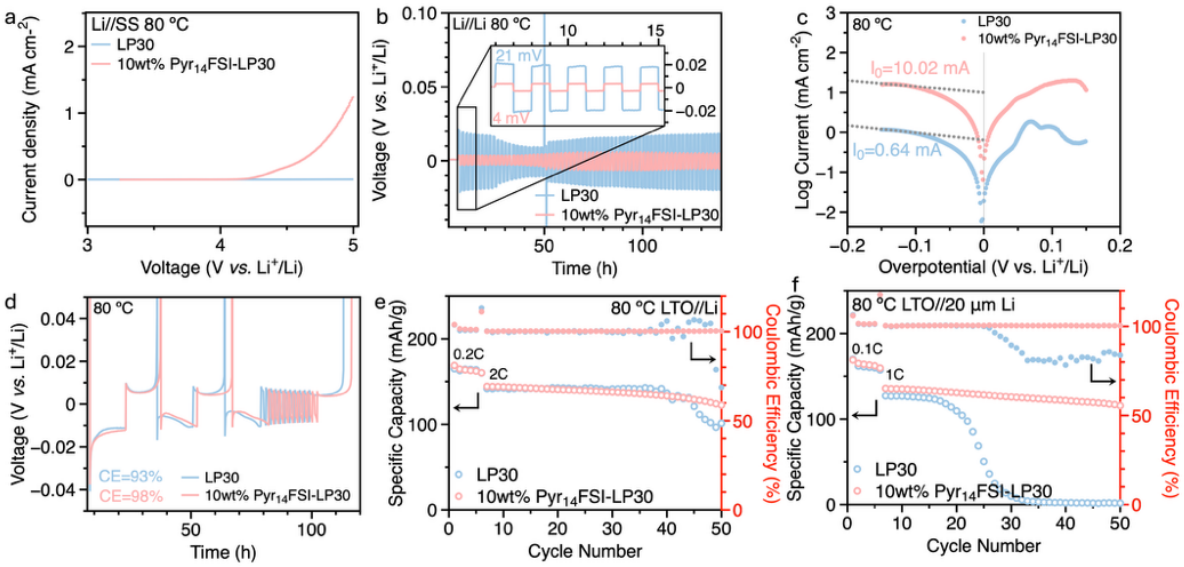

Figure 4.19. Electrochemical performance when using LP30 and $Pyr_{14}FSI$-LP30 as electrolytes at 80 ºC. a) Linear sweep voltammetry in Li//Stainless steel cells at a rate of 1 mV/s. b) Voltage profile of cycling of Li//Li symmetric cells at 0.2 mA cm^{-2}. c) Tafel plot to determine exchange current densities. d) Coulombic efficiency determination in Li//Cu cells. e) Cycling performance of LTO//Li full cells at high rate of 2C (350 mA g^{-1}). f) Extended cycling in LTO//limited Li (20 μm thickness) full cells at 1C (175 mA g^{-1}).

4.8 Ion distribution-diffusion model

To clarify how modified Li^+ coordination by adding $LiNO_3$ and SL enhances electrochemical behavior and SEI quality, we interpret the results through an ion distribution-diffusion model. During charging, the Li-metal surface is negatively charged. In DAIL, Li^+ remains tightly coordinated by multiple anions, and partially desolvated Li^+-$anion_x$ clusters ($x > 1$) carry a net negative charge. These species are electrostatically repelled from the negatively charged interface, while Pyr_{14}^+ cations are drawn toward the surface to maintain charge balance (Figure 4.20, left)[59,60]. As a result, both anions and organic cations undergo reduction, generating a SEI rich in mixed organic-inorganic components. Combined with sluggish Li^+ transport, this leads to interfacial Li^+ depletion at higher currents and produces spatially uneven ion distribution, which promotes irregular deposition, poor CE, and accelerated capacity fade[58,72].

In NS-DAIL, weaker Li^+-anion binding and faster Li^+ transfer enable more complete desolvation at the interface. Consequently, the Li-metal surface is predominantly compensated by freely arriving Li^+ paired with anions, rather than by Pyr_{14}^+ adsorption (Figure 4.20, right)[141,142]. This maintains a uniform and sufficient Li^+ concentration at the surface and directs SEI formation toward an anion-derived, inorganic-rich structure that is mechanically stronger and more ionically conductive. This improved interfacial environment directly supports faster Li^+ diffusion, stabilized plating/stripping, and enhanced cycling performance.

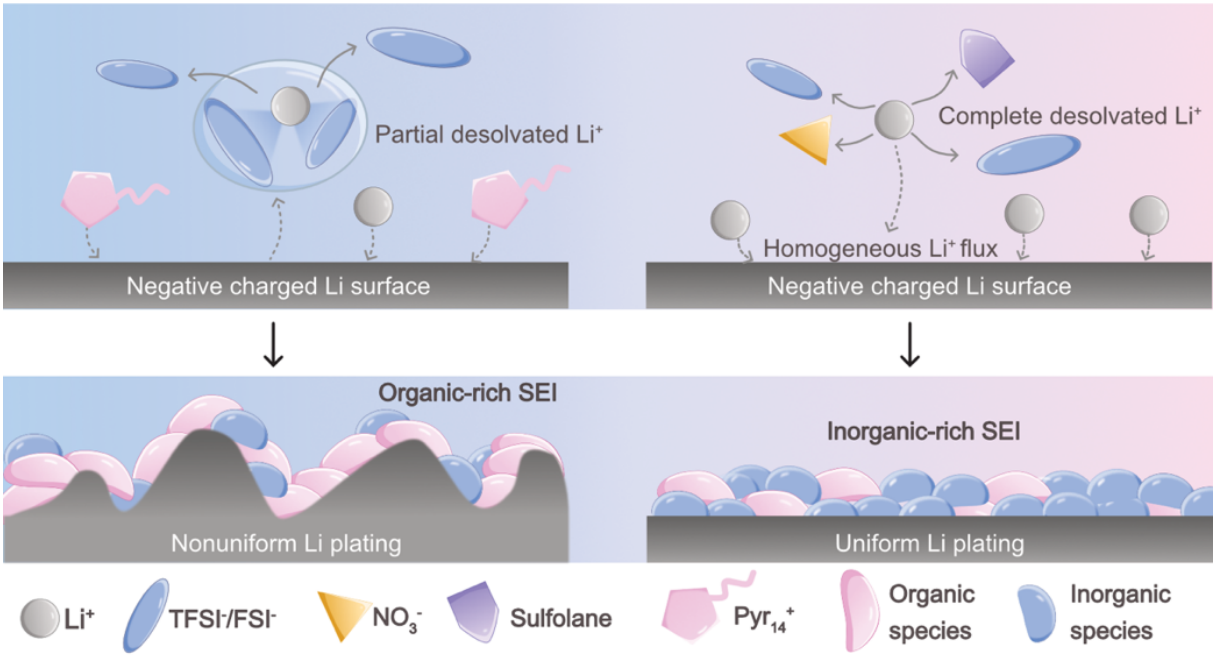

Figure 4.20. Schematic of ion distribution-diffusion model at the Li-metal anode interface, including the desolvation, ion distribution, and SEI composition at the electrolyte/electrode interface of DAIL (left) and NS-DAIL (right).

5 Conclusion and outlook

This work demonstrates electrolyte engineering as a powerful strategy to improve the performance of high-temperature LMBs by regulating solvation structures, ion transfer kinetics, SEI properties, and ionic distribution in EDL. First, the development of a novel $LiNO_3^-$ and SL-added DAIL (NS-DAIL) effectively weakens Li^+-anion coordination, lowers the desolvation barrier, and accelerates charge-transfer kinetics. These improvements yield enhanced rate capability, high coulombic efficiency, and uniform Li plating/stripping, even under demanding high temperature conditions.

Second, introducing $Pyr_{14}FSI$ as an electrolyte additive into carbonate electrolyte LP30 reorganizes the ionic distribution in EDL, where the bulky cations (Pyr_{14}^+) from IL adsorb at the Li surface, delaying local cation depletion, increasing the Sand's time, and suppressing field amplification at protrusions. The growth of dendrite structure becomes both thermodynamically and electrically unfavorable, resulting in uniform and dense Li plating morphologies and ensuring stable cycling of high-temperature LMBs.

Looking forward, the rational design of electrolytes for extreme environments should focus on multi-scale coupling, simultaneously tailoring solvation dynamics, EDL organization, and SEI composition to synergistically regulate charge transfer and interfacial stability. The mechanistic insights revealed here offer a blueprint for next-generation high-temperature electrolytes that balance safety, ionic mobility, and interfacial robustness. Future efforts integrating in-situ/operando characterization and computational modeling will be essential to capture the dynamic evolution of solvation and interfacial chemistry, guiding the predictive design of electrolytes capable of supporting safe, long-life, and high-rate LMBs across a broad temperature range.

Acknowledgements

First and foremost, I would like to express my deepest gratitude to my supervisor, Professor Aleksandar Matic, for his patient guidance, insightful suggestions, and constant encouragement throughout my PhD journey. Thank you for respecting my ideas, giving me the freedom to explore my research, and supporting me in attending international conferences and summer schools. These experiences have not only broadened my academic horizons but also enriched my personal growth. I am especially thankful for your constructive advice and for helping me build collaborations whenever I faced challenges. I feel truly fortunate and grateful to have such a kind and understanding supervisor, who made my transition to life and research in a foreign country much easier and less stressful.

I would also like to express my heartfelt thanks to my former co-supervisor, Professor Shizhao Xiong, for his invaluable guidance both in work and life when I first arrived in Sweden. Thank you for your patience and hands-on help during my initial research period at Chalmers, which helped me adapt smoothly to the new environment.

My sincere thanks also go to Professor Patrik Johansson, my examiner, for his valuable feedback and insightful suggestions on my thesis. I am equally grateful to Dr. Ezio Zhanggellini for his generous help and support in the laboratory. I would like to extend my appreciation to all my collaborators for their guidance and contributions to my research projects. Special thanks to Dr. Nicole Abdou for her help with NMR and the paper, Dr. Amanda Persdotter for her assistance with SEM, and Dr. Carolina Cruz Cardona for her help with MD simulations. I am also thankful to all the KMF colleagues for creating such a friendly and supportive working environment, and to my officemates for bringing so much joy and laughter to everyday life.

Though we are far apart, I am deeply grateful to my parents in China, your constant love, encouragement, and support have always been my strongest motivation. I am thankful to my sister in Spain for her wise advice and constant support in both life and work. Talking with her has always helped me relieve stress and stay optimistic during challenging times. I am also profoundly thankful to my fiancé, Yichen, for his endless companionship, affection, and understanding. I would also like to thank all my friends in Sweden for the wonderful memories we created together, from playing badminton to sharing meals. Those joyful moments have refreshed and energized me during this journey.

Finally, I would like to express my gratitude to the Swedish Electricity Storage and Balancing Centre for funding my research and for organizing inspiring conferences, seminars, and summer schools that greatly enriched my academic experience.

Reference

1. Wang, M., Zheng, M., Lu, J. & You, Y. High-entropy electrolyte toward battery working under extreme conditions. *Joule* **8**, 2467–2482 (2024).
2. Zhang, Y. *et al.* Electrolyte Design for Lithium-Ion Batteries for Extreme Temperature Applications. *Adv. Mater.* **36**, 2308484 (2024).
3. Zhou, Q. *et al.* A Temperature-Responsive Electrolyte Endowing Superior Safety Characteristic of Lithium Metal Batteries. *Adv. Energy Mater.* **10**, 1903441 (2020).
4. Liu, B., Zhang, J.-G. & Xu, W. Advancing Lithium Metal Batteries. *Joule* **2**, 833–845 (2018).
5. Luo, D. *et al.* Electrolyte Design for Lithium Metal Anode-Based Batteries Toward Extreme Temperature Application. *Adv. Sci.* **8**, 2101051 (2021).
6. Heiskanen, S. K., Kim, J. & Lucht, B. L. Generation and Evolution of the Solid Electrolyte Interphase of Lithium-Ion Batteries. *Joule* **3**, 2322–2333 (2019).
7. Wu, H., Jia, H., Wang, C., Zhang, J.-G. & Xu, W. Recent Progress in Understanding Solid Electrolyte Interphase on Lithium Metal Anodes. *Adv. Energy Mater.* **11**, 2003092 (2021).
8. Ding, F. *et al.* Dendrite-Free Lithium Deposition via Self-Healing Electrostatic Shield Mechanism. *J. Am. Chem. Soc.* **135**, 4450–4456 (2013).
9. Sand, H. J. S. III. On the concentration at the electrodes in a solution, with special reference to the liberation of hydrogen by electrolysis of a mixture of copper sulphate and sulphuric acid. *Lond. Edinb. Dublin Philos. Mag. J. Sci.* **1**, 45–79 (1901).
10. Hagopian, A., Doublet, M.-L. & Filhol, J.-S. Thermodynamic origin of dendrite growth in metal anode batteries. *Energy Environ. Sci.* **13**, 5186–5197 (2020).
11. Tikekar, M. D., Choudhury, S., Tu, Z. & Archer, L. A. Design principles for electrolytes and interfaces for stable lithium-metal batteries. *Nat. Energy* **1**, 16114 (2016).
12. Plylahan, N., Kerner, M., Lim, D.-H., Matic, A. & Johansson, P. Ionic liquid and hybrid ionic liquid/organic electrolytes for high temperature lithium-ion battery application. *Electrochimica Acta* **216**, 24–34 (2016).
13. Oltean, G. *et al.* Towards Li-Ion Batteries Operating at 80 °C: Ionic Liquid versus Conventional Liquid Electrolytes. *Batteries* **4**, 2 (2018).
14. Introduction: Ionic Liquids. *Chem. Rev.* **117**, 6633–6635 (2017).
15. Xu, C. *et al.* Locally Concentrated Ionic Liquid Electrolytes for Wide-Temperature-Range Aluminum-Sulfur Batteries. *Angew. Chem.* **136**, e202318204 (2024).
16. Kerner, M., Plylahan, N., Scheers, J. & Johansson, P. Ionic liquid based lithium battery electrolytes: fundamental benefits of utilising both TFSI and FSI anions? *Phys. Chem. Chem. Phys.* **17**, 19569–19581 (2015).
17. Hardacre, C., Holbrey, J. D., Nieuwenhuyzen, M. & Youngs, T. G. A. Structure and Solvation in Ionic Liquids. *Acc. Chem. Res.* **40**, 1146–1155 (2007).

18. Brinkkötter, M., Mariani, A., Jeong, S., Passerini, S. & Schönhoff, M. Ionic Liquid in Li Salt Electrolyte: Modifying the Li+ Transport Mechanism by Coordination to an Asymmetric Anion. *Adv. Energy Sustain. Res.* **2**, 2000078 (2021).

19. Li, N.-W., Yin, Y.-X., Li, J.-Y., Zhang, C.-H. & Guo, Y.-G. Passivation of Lithium Metal Anode via Hybrid Ionic Liquid Electrolyte toward Stable Li Plating/Stripping. *Adv. Sci.* **4**, 1600400 (2017).

20. Hwang, J. *et al.* Ionic liquid electrolyte for room to intermediate temperature operating Li metal batteries: Dendrite suppression and improved performance. *J. Power Sources* **453**, 227911 (2020).

21. Palluzzi, M. *et al.* Ionic Liquids as Cathode Additives for High Voltage Lithium Batteries. *Batter. Supercaps* **7**, e202400068 (2024).

22. Tsurumaki, A. *et al.* Enhanced safety and galvanostatic performance of high voltage lithium batteries by using ionic liquids. *Electrochimica Acta* **316**, 1–7 (2019).

23. Liu, X. *et al.* Difluorobenzene-Based Locally Concentrated Ionic Liquid Electrolyte Enabling Stable Cycling of Lithium Metal Batteries with Nickel-Rich Cathode. *Adv. Energy Mater.* **12**, 2200862 (2022).

24. Liu, X. *et al.* Locally Concentrated Ionic Liquid Electrolyte with Partially Solvating Diluent for Lithium/Sulfurized Polyacrylonitrile Batteries. *Adv. Mater.* **34**, 2207155 (2022).

25. Huang, Y. *et al.* Solvation Structure with Enhanced Anionic Coordination for Stable Anodes in Lithium-Oxygen Batteries. *Angew. Chem. Int. Ed.* **62**, e202306236 (2023).

26. Ma, Y. *et al.* A Modified Sand's Time Incorporating Li-Ion Transport Across the SEI: Basis for Understanding Li Dendrite Formation and Li-Metal Battery Electrolyte Selection. *J. Electrochem. Soc.* **172**, 030506 (2025).

27. Xu, W. *et al.* Lithium metal anodes for rechargeable batteries. *Energy Environ. Sci.* **7**, 513–537 (2014).

28. Zhao, Y. *et al.* Fluorinated ether electrolyte with controlled solvation structure for high voltage lithium metal batteries. *Nat. Commun.* **13**, 2575 (2022).

29. Cheng, X.-B., Zhang, R., Zhao, C.-Z. & Zhang, Q. Toward Safe Lithium Metal Anode in Rechargeable Batteries: A Review. *Chem. Rev.* **117**, 10403–10473 (2017).

30. Wang, D. *et al.* Between Promise and Practice: A Comparative Look at the Energy Density of Li Metal-Free Batteries and Li Metal Batteries. *ACS Energy Lett.* **8**, 5248–5252 (2023).

31. Burton, M. *et al.* Techno-economic assessment of thin lithium metal anodes for solid-state batteries. *Nat. Energy* **10**, 135–147 (2025).

32. Li, S. *et al.* Developing High-Performance Lithium Metal Anode in Liquid Electrolytes: Challenges and Progress. *Adv. Mater.* **30**, 1706375 (2018).

33. Zheng, T. *et al.* Cocktail therapy towards high temperature/high voltage lithium metal battery via solvation sheath structure tuning. *Energy Storage Mater.* **38**, 599–608 (2021).

34. Fan, X. *et al.* Highly Fluorinated Interphases Enable High-Voltage Li-Metal Batteries. *Chem* **4**, 174–185 (2018).

35. Weng, S. *et al.* Temperature-dependent interphase formation and Li+ transport in lithium metal batteries. *Nat. Commun.* **14**, 4474 (2023).

36. Bodenes, L. *et al.* Lithium secondary batteries working at very high temperature: Capacity fade and understanding of aging mechanisms. *J. Power Sources* **236**, 265–275 (2013).

37. Karuppasamy, K. *et al.* Ionic Liquid-Based Electrolytes for Energy Storage Devices: A Brief Review on Their Limits and Applications. *Polymers* **12**, 918 (2020).

38. Schellenberger, M., Golnak, R., Quevedo Garzon, W. G., Risse, S. & Seidel, R. Accessing the solid electrolyte interphase on silicon anodes for lithium-ion batteries in-situ through transmission soft X-ray absorption spectroscopy. *Mater. Today Adv.* **14**, 100215 (2022).

39. Fang, S. *et al.* Enhancing the Interfacial Stability of High-Energy Si/Graphite||$LiNi_{0.88}Co_{0.09}Mn_{0.03}O_2$ Batteries Employing a Dual-Anion Ionic Liquid-based Electrolyte. *Batter. Supercaps* **5**, e202200286 (2022).

40. Wang, L., Zhang, B., Hu, Y., Li, X. & Zhao, T. Failure analysis of LiNi0·83Co0·12Mn0·05O2/graphite–SiOx pouch batteries cycled at high temperature. *J. Power Sources* **482**, 228978 (2021).

41. Jo, C.-H., Sohn, K.-S. & Myung, S.-T. Feasible approaches for anode-free lithium-metal batteries as next generation energy storage systems. *Energy Storage Mater.* **57**, 471–496 (2023).

42. Wang, G. *et al.* Uniform Li deposition regulated via three-dimensional polyvinyl alcohol nanofiber networks for effective Li metal anodes. *Nanoscale* **10**, 10018–10024 (2018).

43. Wu, B. *et al.* Li-growth and SEI engineering for anode-free Li-metal rechargeable batteries: A review of current advances. *Energy Storage Mater.* **57**, 508–539 (2023).

44. Dong, Q. *et al.* A self-adapting artificial SEI layer enables superdense lithium deposition for high performance lithium anode. *Energy Storage Mater.* **45**, 1220–1228 (2022).

45. Lin, L. *et al.* Tailoring Li Deposition by Regulating Structural Connectivity of Electrochemical Li Reservoir in Li-metal Batteries. *Angew. Chem.* **136**, e202319847 (2024).

46. Chen, X.-R., Yan, C., Ding, J.-F., Peng, H.-J. & Zhang, Q. New insights into “dead lithium” during stripping in lithium metal batteries. *J. Energy Chem.* **62**, 289–294 (2021).

47. Li, S. *et al.* Developing High-Performance Lithium Metal Anode in Liquid Electrolytes: Challenges and Progress. *Adv. Mater.* **30**, 1706375 (2018).

48. Liu, Y. *et al.* Electro-Chemo-Mechanical Modeling of Artificial Solid Electrolyte Interphase to Enable Uniform Electrodeposition of Lithium Metal Anodes. *Adv. Energy Mater.* **12**, 2103589 (2022).

49. Fan, L., L. Zhuang, H., Gao, L., Lu, Y. & A. Archer, L. Regulating Li deposition at artificial solid electrolyte interphases. *J. Mater. Chem. A* **5**, 3483–3492 (2017).

50. Shen, X. *et al.* The Failure of Solid Electrolyte Interphase on Li Metal Anode: Structural Uniformity or Mechanical Strength? *Adv. Energy Mater.* **10**, 1903645 (2020).

51. Li, B. *et al.* A Review of Solid Electrolyte Interphase (SEI) and Dendrite Formation in Lithium Batteries. *Electrochem. Energy Rev.* **6**, 7 (2023).

52. Wu, Q., Esping, E. D., Afiandika, M., Xiong, S. & Matic, A. Understanding the electro-chemo-mechanics of lithium metal anodes. *eScience* 100429 (2025) doi:10.1016/j.esci.2025.100429.

53. Xu, Y. *et al.* Promoting Mechanistic Understanding of Lithium Deposition and Solid-Electrolyte Interphase (SEI) Formation Using Advanced Characterization and Simulation Methods: Recent Progress, Limitations, and Future Perspectives. *Adv. Energy Mater.* **12**, 2200398 (2022).

54. Naik, K. G., Vishnugopi, B. S., Datta, J., Datta, D. & Mukherjee, P. P. Electro-Chemo-Mechanical Challenges and Perspective in Lithium Metal Batteries. *Appl. Mech. Rev.* **75**, 010802 (2023).

55. Zhang, W. *et al.* Engineering a passivating electric double layer for high performance lithium metal batteries. *Nat. Commun.* **13**, 2029 (2022).

56. Zhou, T. *et al.* Accelerating Li+/Li redox through the regulation of the electric double layer for efficient lithium metal anodes. *Chem. Eng. J.* **468**, 143676 (2023).

57. Bang, J. *et al.* Regulating electric double-layer dynamics for robust solid-electrolyte interface layer in fast-charging graphite anodes. *J. Mater. Chem. A* **12**, 25254 (2024).

58. He, H. *et al.* Regulating Li-Ion Distribution by the Electrical Double Layer Effect for Dendrite-Free and High-Rate Capability Lithium Metal Batteries. *ACS Appl. Energy Mater.* **5**, 6174–6182 (2022).

59. Wen, Z. *et al.* Dual-Salt Electrolyte Additive Enables High Moisture Tolerance and Favorable Electric Double Layer for Lithium Metal Battery. *Angew. Chem. Int. Ed.* **63**, e202314876 (2024).

60. Xu, R. *et al.* Identifying the Critical Anion–Cation Coordination to Regulate the Electric Double Layer for an Efficient Lithium-Metal Anode Interface. *Angew. Chem. Int. Ed.* **60**, 4215–4220 (2021).

61. Lu, Y. *et al.* Stable Cycling of Lithium Metal Batteries Using High Transference Number Electrolytes. *Adv. Energy Mater.* **5**, 1402073 (2015).

62. Chen, X.-R., Zhao, B.-C., Yan, C. & Zhang, Q. Review on Li Deposition in Working Batteries: From Nucleation to Early Growth. *Adv. Mater.* **33**, 2004128 (2021).

63. Biswal, P., Stalin, S., Kludze, A., Choudhury, S. & Archer, L. A. Nucleation and Early Stage Growth of Li Electrodeposits. *Nano Lett.* **19**, 8191–8200 (2019).

64. Jiao, X. *et al.* Morphology evolution of electrodeposited lithium on metal substrates. *Energy Storage Mater.* **61**, 102916 (2023).

65. Hosseinzadegan, M., Bauer, F., Nyholm, L., Hernández, G. & Maibach, D. R. Separating Nucleation and Growth: High-Overpotential Pretreatment Pulses for Sodium-Metal Electrodes. *Adv. Energy Mater.* **n/a**, e03627.

66. Chang, H. J. *et al.* Correlating Microstructural Lithium Metal Growth with Electrolyte Salt Depletion in Lithium Batteries Using 7Li MRI. *J. Am. Chem. Soc.* **137**, 15209–15216 (2015).

67. Bai, P., Li, J., Brushett, F. R. & Bazant, M. Z. Transition of lithium growth mechanisms in liquid electrolytes. *Energy Environ. Sci.* **9**, 3221–3229 (2016).

68. Cao, W., Li, Q., Yu, X. & Li, H. Controlling Li deposition below the interface. *eScience* **2**, 47–78 (2022).

69. Shen, X. *et al.* The Failure of Solid Electrolyte Interphase on Li Metal Anode: Structural Uniformity or Mechanical Strength? *Adv. Energy Mater.* **10**, 1903645 (2020).

70. Hao, F., Verma, A. & P. Mukherjee, P. Mechanistic insight into dendrite–SEI interactions for lithium metal electrodes. *J. Mater. Chem. A* **6**, 19664–19671 (2018).

71. Kim, J.-M. *et al.* High Current-Density-Charging Lithium Metal Batteries Enabled by Double-Layer Protected Lithium Metal Anode. *Adv. Funct. Mater.* **32**, 2207172 (2022).

72. Zhang, C. *et al.* The Key Role of Anion – Cationic Coordination on Anode Electric-Double-Layer Evolution for High Performance Lithium Metal Battery. *Adv. Funct. Mater.* e10823 (2025) doi:10.1002/adfm.202510823.

73. Liu, S. *et al.* Structure Regulation of Electric Double Layer via Hydrogen Bonding Effect to Realize High-Stability Lithium-Metal Batteries. *ENERGY Environ. Mater.* **7**, e12635 (2024).

74. Fukuda, Y., Tanaka, R. & Ishikawa, M. Beneficial Effects of a Li Salt on Electrode Behavior in an Ionic Liquid for Electric Double Layer Capacitors. *Electrochemistry* **75**, 589–591 (2007).

75. Wu, Q., McDowell, M. T. & Qi, Y. Effect of the Electric Double Layer (EDL) in Multicomponent Electrolyte Reduction and Solid Electrolyte Interphase (SEI) Formation in Lithium Batteries. *J. Am. Chem. Soc.* **145**, 2473–2484 (2023).

76. Groß, A. & Sakong, S. Modelling the electric double layer at electrode/electrolyte interfaces. *Curr. Opin. Electrochem.* **14**, 1–6 (2019).

77. Wu, Q. & Qi, Y. Revealing heterogeneous electric double layer (EDL) structures of localized high-concentration electrolytes (LHCEs) and their impact on solid–electrolyte interphase (SEI) formation in lithium batteries. *Energy Environ. Sci.* **18**, 3036–3046 (2025).

78. Silvester, D. S. *et al.* Electrical Double Layer Structure in Ionic Liquids and Its Importance for Supercapacitor, Battery, Sensing, and Lubrication Applications. *J. Phys. Chem. C* **125**, 13707–13720 (2021).

79. Seo, D. M. *et al.* Reduction Reactions of Carbonate Solvents for Lithium Ion Batteries. *ECS Electrochem. Lett.* **3**, A91–A93 (2014).

80. Stich, M., Göttlinger, M., Kurniawan, M., Schmidt, U. & Bund, A. Hydrolysis of LiPF6 in Carbonate-Based Electrolytes for Lithium-Ion Batteries and in Aqueous Media. *J. Phys. Chem. C* **122**, 8836–8842 (2018).

81. Lee, S. *et al.* Safe, Stable Cycling of Lithium Metal Batteries with Low-Viscosity, Fire-Retardant Locally Concentrated Ionic Liquid Electrolytes. *Adv. Funct. Mater.* **30**, 2003132 (2020).

82. Lin, X. *et al.* Thermally-responsive, nonflammable phosphonium ionic liquid electrolytes for lithium metal batteries: operating at 100 degrees celsius. *Chem. Sci.* **6**, 6601–6606 (2015).

83. Liu, X. *et al.* Reinforcing the Electrode/Electrolyte Interphases of Lithium Metal Batteries Employing Locally Concentrated Ionic Liquid Electrolytes. *Adv. Mater.* **36**, 2309062 (2024).

84. Zhang, H. *et al.* Ionic liquid electrolyte with highly concentrated LiTFSI for lithium metal batteries. *Electrochimica Acta* **285**, 78–85 (2018).

85. Grande, L. *et al.* Homogeneous Lithium Electrodeposition with Pyrrolidinium-Based Ionic Liquid Electrolytes. *ACS Appl. Mater. Interfaces* **7**, 5950–5958 (2015).

86. Kim, J.-K., Matic, A., Ahn, J.-H. & Jacobsson, P. An imidazolium based ionic liquid electrolyte for lithium batteries. *J. Power Sources* **195**, 7639–7643 (2010).

87. Liang, P. *et al.* A Nonflammable High-Voltage 4.7 V Anode-Free Lithium Battery. *Adv. Mater.* **34**, 2207361 (2022).

88. Liu, Q. *et al.* A fluorinated cation introduces new interphasial chemistries to enable high-voltage lithium metal batteries. *Nat. Commun.* **14**, 3678 (2023).

89. Agostini, M. *et al.* A high-power and fast charging Li-ion battery with outstanding cycle-life. *Sci. Rep.* **7**, 1104 (2017).

90. Sun, N. *et al.* Anionic Coordination Manipulation of Multilayer Solvation Structure Electrolyte for High-Rate and Low-Temperature Lithium Metal Battery. *Adv. Energy Mater.* **12**, 2200621 (2022).

91. Yoo, D.-J., Kim, K. J. & Choi, J. W. The Synergistic Effect of Cation and Anion of an Ionic Liquid Additive for Lithium Metal Anodes. *Adv. Energy Mater.* **8**, 1702744 (2018).

92. Zhou, X. *et al.* Anion-Reinforced Solvation for a Gradient Inorganic-Rich Interphase Enables High-Rate and Stable Sodium Batteries. *Angew. Chem. Int. Ed.* **61**, e202205045 (2022).

93. Zhang, G. *et al.* Molecular Design of Competitive Solvation Electrolytes for Practical High-Energy and Long-Cycling Lithium-Metal Batteries. *Adv. Funct. Mater.* **34**, 2312413 (2024).

94. Wang, X. *et al.* Hybrid Electrolyte with Dual-Anion-Aggregated Solvation Sheath for Stabilizing High-Voltage Lithium-Metal Batteries. *Adv. Mater.* **33**, 2007945 (2021).

95. Zhou, P., Xiang, Y. & Liu, K. Understanding and applying the donor number of electrolytes in lithium metal batteries. *Energy Environ. Sci.* **17**, 8057–8077 (2024).

96. Gu, R. *et al.* An Ether-Based Electrolyte Solvation Strategy for Long-Term Stability and Ultra-Low Temperature Li-Metal Batteries. *Adv. Funct. Mater.* **34**, 2310747 (2024).

97. Zhang, X.-Q. *et al.* Highly Stable Lithium Metal Batteries Enabled by Regulating the Solvation of Lithium Ions in Nonaqueous Electrolytes. *Angew. Chem. Int. Ed.* **57**, 5301–5305 (2018).

98. Jiang, G. *et al.* Perspective on High-Concentration Electrolytes for Lithium Metal Batteries. *Small Struct.* **2**, 2000122 (2021).

99. Chen, S. *et al.* High-Voltage Lithium-Metal Batteries Enabled by Localized High-Concentration Electrolytes. *Adv. Mater.* **30**, 1706102 (2018).

100. Yoo, D.-J., Yang, S., Kim, K. J. & Choi, J. W. Fluorinated Aromatic Diluent for High-Performance Lithium Metal Batteries. *Angew. Chem. Int. Ed.* **59**, 14869–14876 (2020).

101. Ishfaq, H. A. *et al.* Enhanced performance of lithium metal batteries via cyclic fluorinated ether based electrolytes. *Energy Storage Mater.* **69**, 103375 (2024).

102. Nakanishi, A. *et al.* Sulfolane-Based Highly Concentrated Electrolytes of Lithium Bis(trifluoromethanesulfonyl)amide: Ionic Transport, Li-Ion Coordination, and Li–S Battery Performance. *J. Phys. Chem. C* **123**, 14229–14238 (2019).

103. Li, P., Zhang, H., Lu, J. & Li, G. Low Concentration Sulfolane-Based Electrolyte for High Voltage Lithium Metal Batteries. *Angew. Chem. Int. Ed.* **62**, e202216312 (2023).

104. Fu, J. *et al.* Lithium Nitrate Regulated Sulfone Electrolytes for Lithium Metal Batteries. *Angew. Chem.* **132**, 22378–22385 (2020).

105. Wu, F. *et al.* Dual-anion ionic liquid electrolyte enables stable Ni-rich cathodes in lithium-metal batteries. *Joule* **5**, 2177–2194 (2021).

106. Zhu, Y. *et al.* Multifunctional Electrolyte Additives for Better Metal Batteries. *Adv. Funct. Mater.* **34**, 2301964 (2024).

107. Ding, F. *et al.* Effects of Carbonate Solvents and Lithium Salts on Morphology and Coulombic Efficiency of Lithium Electrode. *J. Electrochem. Soc.* **160**, A1894 (2013).

108. Park, M. S. *et al.* A Highly Reversible Lithium Metal Anode. *Sci. Rep.* **4**, 3815 (2014).

109. Zhang, X.-Q. *et al.* Columnar Lithium Metal Anodes. *Angew. Chem. Int. Ed.* **56**, 14207–14211 (2017).

110. Dalavi, S., Xu, M., Knight, B. & Lucht, B. L. Effect of Added LiBOB on High Voltage (LiNi0.5Mn1.5O4) Spinel Cathodes. *Electrochem. Solid-State Lett.* **15**, A28 (2011).

111. Xu, M. *et al.* Investigation and application of lithium difluoro(oxalate)borate (LiDFOB) as additive to improve the thermal stability of electrolyte for lithium-ion batteries. *J. Power Sources* **196**, 6794–6801 (2011).

112. Shi, F. *et al.* Strong texturing of lithium metal in batteries. *Proc. Natl. Acad. Sci.* **114**, 12138–12143 (2017).

113. Guo, J., Wen, Z., Wu, M., Jin, J. & Liu, Y. Vinylene carbonate–LiNO3: A hybrid additive in carbonic ester electrolytes for SEI modification on Li metal anode. *Electrochem. Commun.* **51**, 59–63 (2015).

114. Lee, J. Z. *et al.* Cryogenic Focused Ion Beam Characterization of Lithium Metal Anodes. *ACS Energy Lett.* **4**, 489–493 (2019).

115. Jones, R. R., Hooper, D. C., Zhang, L., Wolverson, D. & Valev, V. K. Raman Techniques: Fundamentals and Frontiers. *Nanoscale Res. Lett.* **14**, 231 (2019).

116. Fujimori, T. *et al.* Conformational structure of room temperature ionic liquid *N*-butyl-*N*-methyl-pyrrolidinium bis(trifluoromethanesulfonyl) imide — Raman spectroscopic study and DFT calculations. *J. Mol. Liq.* **131–132**, 216–224 (2007).

117. Haneke, L. *et al.* Editors' Choice—Mechanistic Elucidation of Anion Intercalation into Graphite from Binary-Mixed Highly Concentrated Electrolytes via Complementary 19F MAS NMR and XRD Studies. *J. Electrochem. Soc.* **167**, 140526 (2020).

118. Celeste, A. *et al.* Enhancement of Functional Properties of Liquid Electrolytes for Lithium-Ion Batteries by Addition of Pyrrolidinium-Based Ionic Liquids with Long Alkyl-Chains. *Batter. Supercaps* **3**, 1059–1068 (2020).

119. Pitawala, J., Martinelli, A., Johansson, P., Jacobsson, P. & Matic, A. Coordination and interactions in a Li-salt doped ionic liquid. *J. Non-Cryst. Solids* **407**, 318–323 (2015).

120. Mukai, K., Inoue, T., Kato, Y. & Shirai, S. Superior Low-Temperature Power and Cycle Performances of Na-Ion Battery over Li-Ion Battery. *ACS Omega* **2**, 864–872 (2017).

121. *Thermal Analysis of Polymers*. (John Wiley & Sons, Ltd, 2009). doi:10.1002/9780470423837.

122. Ferreira, E. B., Lima, M. L. & Zanotto, E. D. DSC Method for Determining the Liquidus Temperature of Glass-Forming Systems. *J. Am. Ceram. Soc.* **93**, 3757–3763 (2010).

123. Pitawala, J. *et al.* Phase behaviour, transport properties, and interactions in Li-salt doped ionic liquids. *Faraday Discuss* **154**, 71–80 (2012).

124. Otto, S.-K. *et al.* In-Depth Characterization of Lithium-Metal Surfaces with XPS and ToF-SIMS: Toward Better Understanding of the Passivation Layer. *Chem. Mater.* **33**, 859–867 (2021).

125. Xu, C. *et al.* Interface layer formation in solid polymer electrolyte lithium batteries: an XPS study. *J. Mater. Chem. A* **2**, 7256–7264 (2014).

126. Oswald, S. *et al.* Binding Energy Referencing for XPS in Alkali Metal-Based Battery Materials Research (II): Application to Complex Composite Electrodes. *Batteries* **4**, 36 (2018).

127. Liu, Y. *et al.* Insight into the Critical Role of Exchange Current Density on Electrodeposition Behavior of Lithium Metal. *Adv. Sci.* **8**, 2003301 (2021).

128. Wang, S. *et al.* Electrochemical impedance spectroscopy. *Nat. Rev. Methods Primer* **1**, 1–21 (2021).

129. Wang, P. *et al.* Study of the formation and evolution of solid electrolyte interface via in-situ electrochemical impedance spectroscopy. *Appl. Surf. Sci.* **596**, 153572 (2022).

130. Chapter 3 Linear Sweep and Cyclic Voltammetry. in *Comprehensive Chemical Kinetics* vol. 26 145–202 (Elsevier, 1986).

131. Kissinger, P. T. & Heineman, W. R. Cyclic voltammetry. *J. Chem. Educ.* **60**, 702–706 (1983).

132. Adams, B. D., Zheng, J., Ren, X., Xu, W. & Zhang, J.-G. Accurate Determination of Coulombic Efficiency for Lithium Metal Anodes and Lithium Metal Batteries. *Adv. Energy Mater.* **8**, 1702097 (2018).

133. Li, Y. *et al.* A progressive nucleation mechanism enables stable zinc stripping–plating behavior. *Energy Environ. Sci.* **14**, 5563–5571 (2021).

134. Lai, Y., Liu, F., Li, J., Zhang, Z. & Liu, Y. Nucleation and growth of selenium electrodeposition onto tin oxide electrode. *J. Electroanal. Chem.* **639**, 187–192 (2010).

135. Rey, I. *et al.* Spectroscopic and Theoretical Study of (CF3SO2)2N- (TFSI-) and (CF3SO2)2NH (HTFSI). *J. Phys. Chem. A* **102**, 3249–3258 (1998).

136. Barghamadi, M. *et al.* Effect of LiNO3 additive and pyrrolidinium ionic liquid on the solid electrolyte interphase in the lithium–sulfur battery. *J. Power Sources* **295**, 212–220 (2015).

137. Xu, X. *et al.* Role of Li-Ion Depletion on Electrode Surface: Underlying Mechanism for Electrodeposition Behavior of Lithium Metal Anode. *Adv. Energy Mater.* **10**, 2002390 (2020).

138. Hernandez-Maya, R., Rosas, O., Saunders, J. & Castaneda, H. Dynamic Characterization of Dendrite Deposition and Growth in Li-Surface by Electrochemical Impedance Spectroscopy. *J. Electrochem. Soc.* **162**, A687 (2015).

139. Liu, J. *et al.* Distinct Differences in Li-Deposition/Dissolution Reversibility in Sulfolane-Based Electrolytes Depending on Li-Salt Species and Their Solvation Structures. *J. Phys. Chem. C* **127**, 5689–5701 (2023).

140. Tułodziecki, M., Tarascon, J.-M., Taberna, P.-L. & Guéry, C. Catalytic reduction of TFSI-containing ionic liquid in the presence of lithium cations. *Electrochem. Commun.* **77**, 128–132 (2017).

141. Zhang, W. *et al.* Engineering a passivating electric double layer for high performance lithium metal batteries. *Nat. Commun.* **13**, 2029 (2022).

142. Yuan, X. *et al.* Engineering battery corrosion films by tuning electrical double layer composition. *Joule* **8**, 3038–3053 (2024).